Water flow timing, quantity, and sources in a fractured high mountain permafrost rock wall

Matan Ben-Asher[1], Antoine Chabas[2], Jean-Yves Josnin[2], Josué Bock[2], Emmanuel Malet[2], Amaël Poulain[3], Yves Perrette[2], Florence Magnin[2]

[1] Department of Natural Sciences, Open University of Israel, Ra'anana, Israel

[2] EDYTEM, USMB, CNRS, 5 bd de la mer Caspienne, 73376 Le Bourget du Lac cedex, France

[3] TRAQUA S.A., Namur, Belgium

Correspondence to: Matan Ben-Asher (matanbe@openu.ac.il) and Florence Magnin (Florence.Magnin@univ-smb.fr)

Abstract

Water flow in high mountain rock walls is crucial ~~in~~for landscape evolution and slope stability. However, the timing, quantity, and sources of this flow remain poorly understood. In the Mont Blanc massif, tunnels at the Aiguille du Midi peak (3842 m) provide direct access to steep permafrost-affected rock walls. ~~Over two years (~~Between May 2022~~–~~ and October 2023~~),~~ we monitored water flowing from fractures using a real-time system ~~measuring~~that measured flow rate, temperature, electrical conductivity, and ~~fluorescent~~fluorescence of tracers, ~~together with~~alongside meteorological data and ground surface temperatures.

~~Results~~The results indicate high surface–subsurface connectivity. The water source is primarily snowmelt, with additional inputs from late-summer rainfall. Electrical conductivity, stable isotopes, and recession curve analysis suggest another source of older subsurface ice. Flow onset was closely tied to ~~ATs~~air temperatures, with steady diurnal fluctuations appearing once ~~ground~~rock surface temperatures exceeded ~~0~~0 °C. Lag times between daily peaks of flow rate and peaks of air and ground surface temperatures of 3~~–9 hours~~9 hours and 0~~–3 hours~~3 hours, respectively, point to rapid unsaturated infiltration conditions. Distinct flow regimes observed in two adjacent fracture systems reflect a complex, heterogeneous network, including sediment-filled fractures with a delayed response. Significant flow ~~rate~~rates (often >10 L/h) and water temperature often exceeding 5 °C, suggest~~a~~ significant heat transfer by advection, capable of enhancing permafrost degradation.

This study provides rare direct observations of fracture flow dynamics in steep permafrost rocks, ~~improving~~and improves our understanding of water routing and its response to atmospheric forcing. The findings offer valuable constraints for coupled hydrothermal models, permafrost-related hazard assessments, and the potential impact of climate change.

Key words: Permafrost, monitoring, water infiltration, Mont Blanc massif, climate change

1. Introduction

1.1. Hydrogeology of high mountains

Water plays a crucial role in weathering and erosion processes in mountainous landscapes. In the periglacial belt, the presence of water in the shallow subsurface can ~~lead to~~cause rock fracturing through ice segregation or volumetric expansion, depending on temperature conditions and saturation levels (Draebing and Krautblatter, 2019; Matsuoka and Murton, 2008). ~~Hydrostatic pressure in undrained fractures is capable of driving catastrophic failure (Hasler et al., 2012; Krautblatter et al., 2013a; Scandroglio et al., 2021).~~Hydrostatic pressure in undrained fractures can drive catastrophic failure (Hasler et al., 2012; Krautblatter et al., 2013; Scandroglio et al., 2021; Walter et al., 2020). Over geological time scales water is a key catalyst of mechanical rock weathering processes related to subcritical cracking (Eppes and Keanini, 2017). The melting of ice in joints under thawing conditions ~~releases~~can release detached blocks and lead to debris and ~~boulders~~rock falls, and the formation of scree slopes (Hales and Roering, 2007). Water infiltration in bedrock may also trigger large ~~destabilizations such as rockfalls and~~ rock ~~avalanches~~slope failures by reducing the friction of rough fracture contact surfaces ~~(Krautblatter et al., 2013a). In permafrost ground, the presence of ice sealing in the ground interstices~~(Krautblatter et al., 2013). In permafrost ground, the presence of sealing ice in pores and fractures favors the development of high hydrostatic pressures (Fischer et al., 2010; Marcer et al., 2020), ~~possibly enhancing~~which may increase the frequency or magnitude of mass movements. In addition to mechanical pressure, water circulation can also cause thermal perturbations with potential cooling effects in some cases ~~(Maréchal et al., 1999) or warming effects in others (Hasler et al., 2011).~~(Maréchal et al., 1999; Phillips et al., 2016) or warming effects in others (Hasler et al., 2011; Phillips et al., 2016). In permafrost ground, heat advection from water infiltration could accelerate permafrost degradation (Gruber and Haeberli, 2007; Hasler et al., 2011; Magnin and Josnin, 2021), and potentially develop thawing corridors (Krautblatter and Hauck, 2007; Keushing et al., 2017). Recent observations of increased rock fall activity in high mountains regions ~~was~~have been linked ~~with~~to permafrost degradation (Allen et al., 2009; Fey et al., 2025; Gruber et al., 2004; Huggel et al., 2012; Legay et al., 2021; Ravanel et al., 2017; Ravanel and Deline, 2011). ~~The warming of intact frozen rock is commonly related to rockwall destabilization through the decrease of the rock uniaxial and tensile strength (Dwivedi et al., 1998; Krautblatter et al., 2013a; Li et al., 2003; Mellor, 1973; Scandroglio et al., 2025). Water related processes were suggested as a potential mechanistic driver~~The warming of intact frozen rock is commonly related to rockwall destabilization due to a decrease in rock uniaxial and tensile strength (Dwivedi et al., 1998; Krautblatter et al., 2013; Li et al., 2003; Mellor, 1973). Water-related processes have been suggested as a potential cause of several rock fall events (Cathala et al., 2024; Erismann and Abele, 2001; Scandroglio et al., 2021; Strauhal et al., 2016). ~~However, while hydrogeological studies in alpine permafrost have primarily focused on coarse-grained terrains such as rock glaciers and scree slopes,~~However, while hydrogeological studies in alpine permafrost have primarily focused on coarse-grained terrain, such as rock glaciers (Bast et al., 2024) and scree slopes (Pellet and Hauck, 2017), little is known about water dynamics within bedrock rockwalls—despite their critical role in slope stability and landscape evolution.

1.2. Existing knowledge on water flow and infiltration in mountain permafrost

In steep alpine bedrock, the question of water infiltration and its thermal and mechanical implications is crucial but is rarely addressed directly ~~(Krautblatter et al., 2013b). Studying hydrogeological processes in these environments presents~~(Krautblatter et al., 2013). Studying hydrogeological processes in these environments poses several challenges, including limited accessibility, the hidden nature of water flow pathways, strong spatial and temporal variability, non-linear system behavior, and the difficulty of ~~quantitatively~~ identifying water sources quantitatively. Hasler et al. (2011) used numerical simulations to explore the impact of advective heat transport by water percolation on subsurface temperatures and ice-level changes. In the absence of hydrogeological field measurements, they performed laboratory experiments and ~~were able to show~~demonstrated significant implications for the role of water flow in thaw-related instabilities in cold mountain permafrost regions. Maréchal et al. (1999) used a hydrothermal model to simulate an observed thermal anomaly that was found during drilling work in the road tunnel under the Mont-Blanc massif and showed that infiltration of ~~waters~~water from the surface contributed to the continuous cooling of the alpine massif at depth. Ben-Asher et al. (2023) estimated the potential water input in steep alpine bedrock using field measurements and numerical simulations.

~~Other than~~Apart from indirect studies (Ben-Asher et al., 2023; Hasler et al., 2011; Maréchal et al., 1999; Scherler et al., 2010), ~~very~~ few studies have attempted to directly monitor groundwater flow in steep ~~and high alpine~~, permafrost-affected alpine environments (Gabrielli et al., 2012; Manning and Caine, 2007). In a recent study, Scandroglio et al. (2025) measured water outflow in 55 m deep fractures under the permafrost-affected Zugspitze Ridge (2815–2962 m ~~asl~~a.s.l). They compared their dataset with meteorological data and a snowmelt model to infer ~~hydrological properties~~the timing and quantity of water flow and constrain the hydrological pressure in the fractures. They also analyzed recession curves of the measured flow rate, a technique that was never applied to alpine rock fractures before.

1.3. Saturated and non-saturated flow

From a hydrogeological perspective, a fractured summit is ~~rather characterized~~more accurately described as a permeable infiltration zone than as an aquifer. However, due to the scarcity of drilling data, constraints on the thickness of the high-~~altitude~~elevation alpine unsaturated zone remain highly limited (Maréchal, 1998). The first tests of hydrodynamical models of a high alpine and permafrost-affected rock wall site were performed by Magnin & Josnin (2021) on the Aiguille du Midi site. This study ~~has shown~~showed that the unsaturated zone is probably more than 1000 m thick. In the Rocky Mountains, several hundred meters of unsaturated zone above the water table have also been reported (Russell et al. 2001).

Generally, unsaturated conditions apply in soils, permeable rocks, and deposits, and water flow is often considered subvertical and evaluated using the Richards equation (Smith, 2002). In crystalline rock settings, porosity and permeability are essentially controlled by the geometry of the ~~fractures~~fracture network, where most of the water flow ~~takes place~~occurs. The water flow in fractures is thus not uniform but occurs along preferential flow paths sometimes called “fingers” (Su et al., 2000), that

channel the flow path at the larger scale of the fractured medium (Tsang et al., 2013). These preferential flow paths ~~are~~have been observed in both ~~in~~ saturated and unsaturated fractures (Su et al., 2000).

In the study area of the Mont-Blanc massif, the fracture network opening is highly irregular (~~millimeters to decimeters depending on the fractures) and expected to evolve seasonally~~from millimeters to decimeters, depending on the fractures) and is expected to evolve seasonally, with reversible opening in winter (Guillet et al., 2018), superimposed on an irreversible long-term opening trend (Weber et al., 2017). The fractures can also be affected by the water flow~~-~~, which can change the extent of ice filling~~, or plugging~~ and develop partially saturated conditions similar to those known from some epikarsts (Ford and Williams, 1989).

This study is motivated by the need to better understand hydrological processes in high mountain permafrost environments and connectivity with changing surface conditions, particularly in the context of ongoing climate change. We aim to ~~fill~~address major knowledge gaps ~~about~~in the hydrology of high-elevation permafrost rock regarding the timing ~~and~~, quantity, and source of water flow ~~from the surface to~~in the fractures, and how the flow is affected by surface conditions ~~at the surface~~ and the source of infiltrating water.

2. Study site and meteorological context

2.1. Aiguille du Midi site

The Aiguille du Midi (AdM) is a peak composed of three granite pillars - Piton Nord, Piton Central, and Piton Sud~~, with the~~. The central pillar (Piton Central) ~~reaching~~reaches an elevation of 3842 m ~~asl~~a.s.l and ~~towering~~towers approximately 3000 m above the valley of Chamonix (Figure 1~~). The site lies on the NW flank of the Mont Blanc massif (MBM) that covers an area of about 550 km² and is oriented NW-SE between France, Italy, and Switzerland. It is a part of the external crystalline massif of the Alps, whose uplift started about 22 Myr ago (Leloup et al., 2005). It is composed of two main lithological units: a Variscan metamorphic series (mostly gneisses and mafic schists) (453 ± 3 Ma) on the W and S side, and an intrusion of calc-alkaline granite (304 ± 3 Ma) with aplitic veins (Raumer and Bussy, 2004). The MBM is crosscut by a network of shear zones and faults that are mostly oriented N–S and dip sub-vertically (Rossi et al., 2005). Across the NW–SE transect of the massif, these shear zones show a fan geometry, verging NW on the NW part of the massif, and SE on the SE (Bertini et al., 1985), which delineates the main topographical features. High and steep granite rock faces and peaks are typical of the MBM that hosts 28 summits above 4000 m asl, including the roof of the European Alps: the Mont Blanc whose ice cap reached 4805 m asl in 2023.~~

~~). The site lies on the NW flank of the Mont Blanc massif (MBM) which covers an area of about 550 km² and is oriented NW-SE between France, Italy, and Switzerland.~~

Glaciers occupied about 100 km² in the late 2000s (Gardent et al., 2014) while permafrost is largely present above ~~roughly~~approximately 2600 m in N faces and 3200 m in S faces (Magnin et al., 2015a).

The combination of steepness, permafrost, and glacial dynamics results in highly active morphodynamics (Deline et al., 2015). Over the past decades, rockfall (volume > 100 m^3) frequency has significantly increased (Ravanel and Deline, 2011), notably during the hot summers. The main cause ~~was~~has been suggested to be permafrost degradation (Ravanel et al., 2017; Legay et al., 2021; Magnin et al., 2023). Permafrost investigation started in the mid-2000s in the MBM, with the installation of various temperature sensors in AdM (Magnin et al., 2015b), including 10-m deep boreholes, which ~~registered~~recorded a temperature increase ~~>~~of over 1 °C during the 2011-2020 decade (Magnin et al., 2024).

AdM has been chosen as a pilot site for alpine permafrost investigations because of its representativeness of high alpine rockwalls and its accessibility from Chamonix by a cable-car. Man-made ~~galleries~~tunnels, terraces, bridges, and an elevator allow the visitors to access different parts of the site. Since the hot summer of 2015, water flowing from the fractured ~~gallery~~tunnel walls has become a problem for the operating company (the *Compagnie du Mont Blanc*), leading to the installation of a drained metal plate ceiling to divert the flowing water and keep some parts of the ~~galleries~~tunnels dry for visitors.

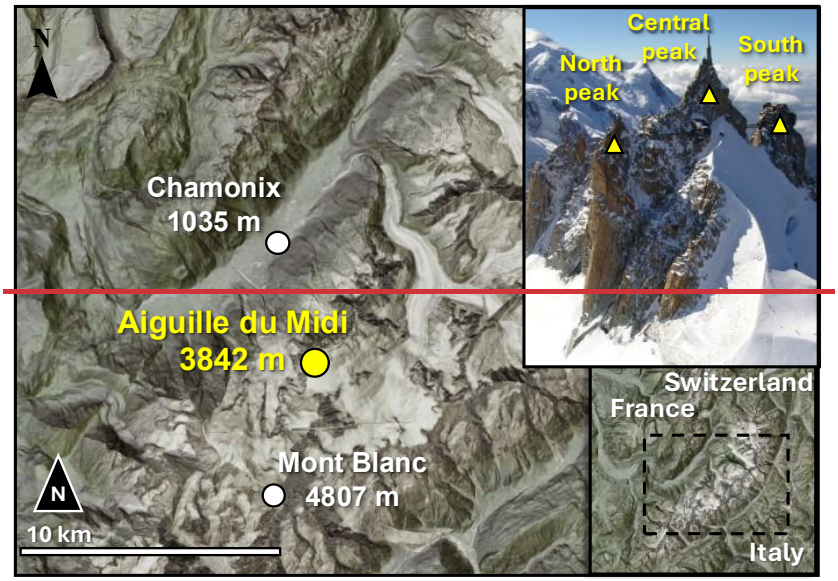
N
Chamonix
1035 m
Aiguille du Midi
3842 m
Mont Blanc
4807 m
N
10 km
Central
peak
North
peak
South
peak
Switzerland
France
Italy

136

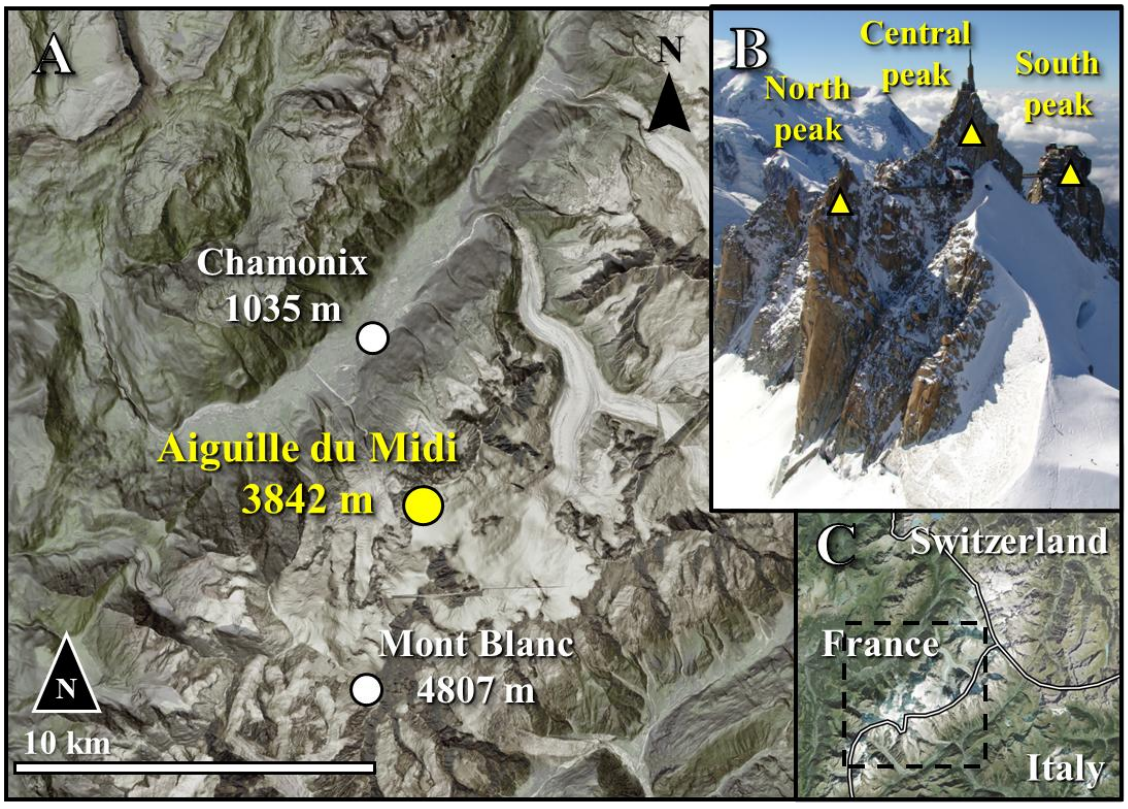
A
N
Chamonix
1035 m
Aiguille du Midi
3842 m
Mont Blanc
4807 m
N
10 km
B
Central
peak
North
peak
South
peak
C
Switzerland
France
Italy

137

Figure 1: A) Location of the Aiguille du Midi in the Mont Blanc massif ~~and~~. B) view of the three peaks at Aiguille du Midi. (Picture: S. Gruber~~.~~). C) Location of the Mont Blanc massif on the border of France, Italy and Switzerland. Maps provided by the Swiss Federal Office of Topography swisstopo.

2.2. Meteorological conditions in 2022 and 2023

~~In~~ As of 2024, in Europe, the years 2022 and 2023~~, respectively,~~ were the third and second warmest years in ~~records,~~record after 2020, respectively, with a mean annual air temperature (~~AT) being~~MAAT) about 1.1 °C above the 1991-2020 average (ESOTC 2023, 2024). Summer 2022 was the warmest summer ever recorded, outpacing the 1991-2020 average by 1.4°C (ESOTC, 2023). September 2023 was the warmest September on record (EOSTC, 2023).

Air temperature (AT) and precipitation records in the town of Chamonix (France), located in the valley just north of AdM~~,~~ ~~started~~ (Fig. 1), began in the early 20th century and are well-suited to characterize the local precipitation regime. At ~~the~~ AdM, AT records started in 2007 but are affected by numerous gaps that sometimes last several months, making this data less reliable for multi-annual comparison.

Figure 2 shows AT ~~in AdM~~ and precipitation in Chamonix~~, from 2022~~ and at AdM for 2022–2023 ~~are displayed in~~ Figure 2. ~~In 2022, winter~~Winter and early spring ~~(January–April)~~2022 were ~~drier (198 and 405 mm recorded at Chamonix over January–April) and~~ markedly warmer ~~(+1.4 °C)~~and drier than in 2023, with ~~an average of 10.9°C and 12.3°C respectively~~mean AT at ~~the~~ AdM~~.~~ about 1.4 °C higher and precipitation roughly half as much. A late~~-~~spring heat wave ~~led to the warmest~~ produced a record high AT in May ~~ever recorded in Chamonix with a temperature anomaly of +2.6 °C compared to the 1993~~–2022 ~~period (continuous hourly records started in 1993 in Chamonix),~~ while May 2023 was near average. ~~The mean ATs in June–August~~Summer conditions were ~~similar for both years. The~~generally warmer in 2022, but an exceptional late ~~summer~~-season heat wave ~~in 2023 led to the warmest~~ occurred in September ~~ever recorded in Chamonix with a temperature anomaly of +3.1 °C compared to the 1993–2022 period, while~~2023—the warmest on record in Chamonix—whereas September 2022 was ~~average. Precipitation in spring 2022 was less than half of that in~~near normal. Overall, 2023 ~~(184 and 418 mm, respectively, over March–May) while summer 2023 was only slightly~~ was wetter than ~~in 2022 (+ 32 mm over June–August). June and September 2022 were wetter than in 2023 and July and August 2023 were wetter than in 2022. Autumn 2023 was also wetter than 2022 (+168 mm over September–November).~~2022, mainly due to higher precipitation in spring and autumn.

In summary, 2022 was characterized by a very early but long-lasting and record-breaking summer heat wave, while 2023 was characterized by a late and record-breaking summer heat wave with significantly more precipitation than in 2022.

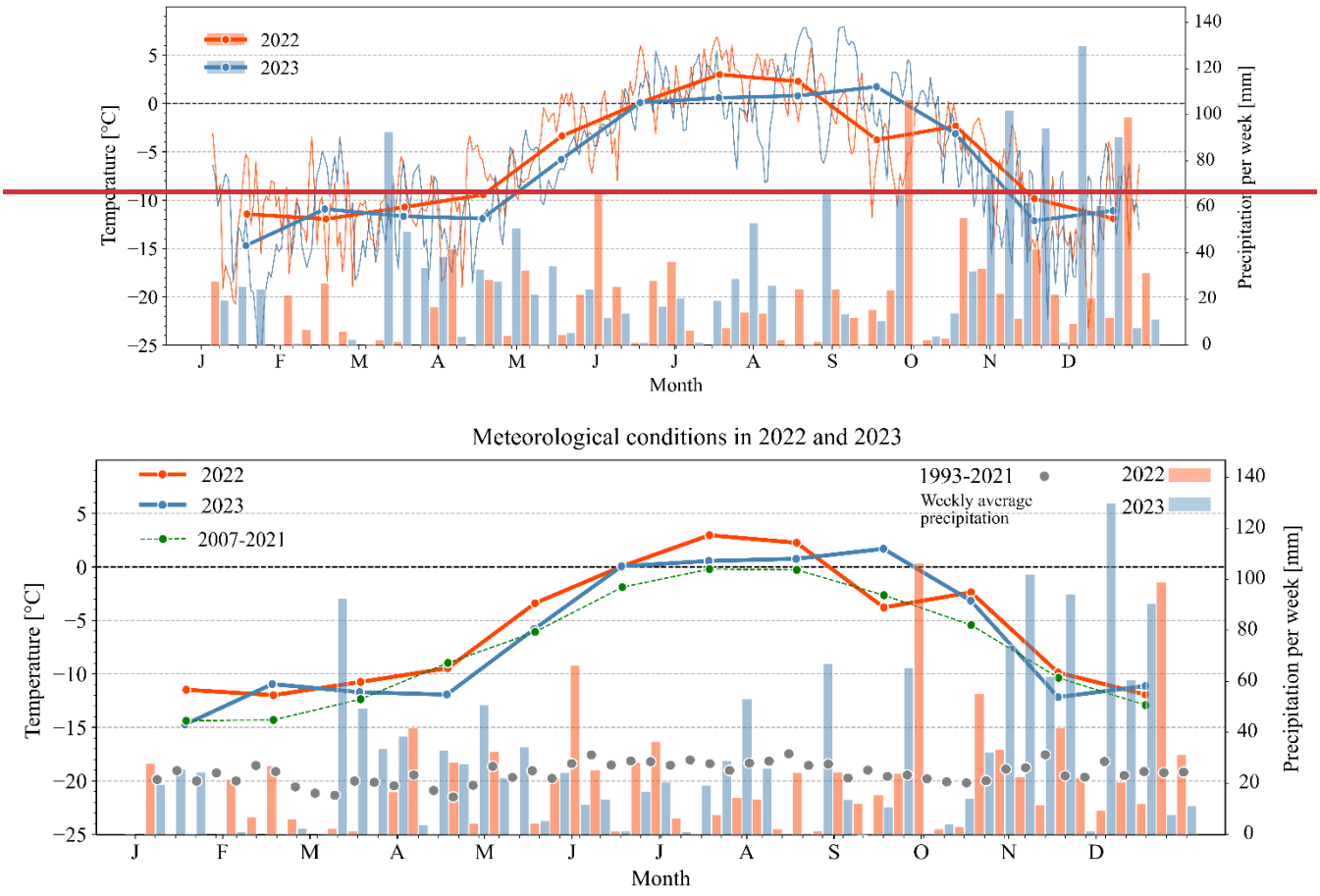

Figure 2: ~~Daily (thin lines~~Monthly average air temperatures (Lines) and ~~monthly (thick lines) air temperature and~~ weekly precipitation (bars) in 2022 (orange) and 2023 (~~bars~~blue). Air temperature was measured at the ~~top of the~~site in Aiguille du Midi ~~and precipitation~~ (3842 m a.s.l). Precipitation was measured in Chamonix (1042 m ~~asl),~~a.s.l), since no reliable precipitation data is available at the high elevation site. Data provided by Météo France. The long-term average air temperature (2007-2021) is presented as a green thin dashed line. The long-term average weekly precipitation in Chamonix (1993-2021) is shown by gray circles.

~~3. Method~~

3. Methods

In April and May 2022-, we installed a monitoring system ~~was installed~~ to measure characteristics of water flowing through fractures in the roof of the ~~gallery~~tunnel in AdM (Figure 3, Figure 4). ~~Fluorescent dyes were poured into the snowpack on the rock face above the gallery to trace the water. Ground Surface Temperature (GST) sensors were installed on the rock surface, below and around the snowpack where fluorescent dyes were inserted. Figure 3 illustrates the entire methodological approach of the monitoring system.~~

181

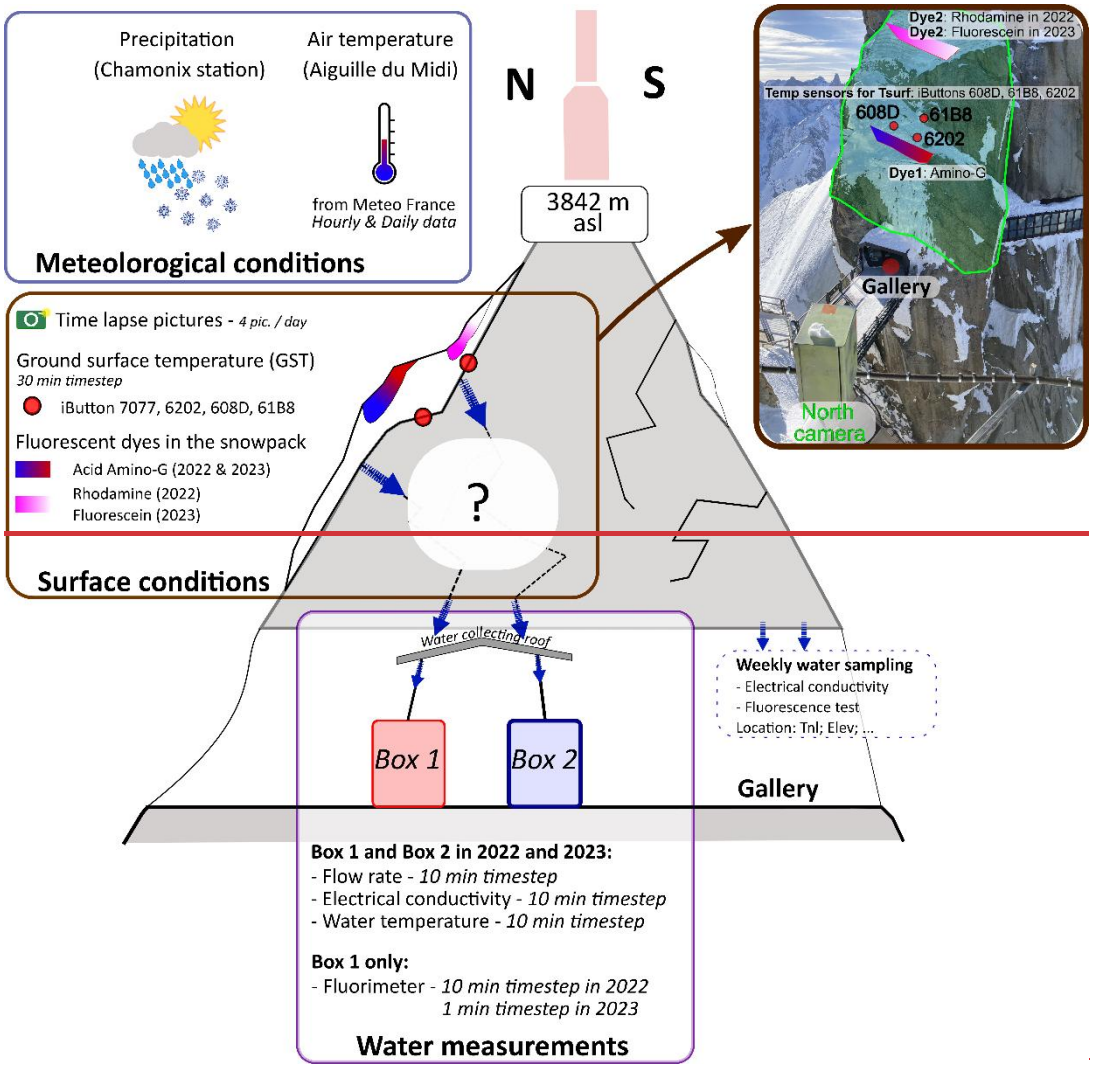
Precipitation
(Chamonix station)
Air temperature
(Aiguille du Midi)
from Meteo France
Hourly & Daily data
Meteorological conditions
N
S
3842 m asl
Dye2: Rhodamine in 2022
Dye2: Fluorescein in 2023
Temp sensors for Tsurf: iButtons 608D, 61B8, 6202
608D
61B8
6202
Dye1: Amino-G
Gallery
North camera
Time lapse pictures - 4 pic. / day
Ground surface temperature (GST)
30 min timestep
iButton 7077, 6202, 608D, 61B8
Fluorescent dyes in the snowpack
Acid Amino-G (2022 & 2023)
Rhodamine (2022)
Fluorescein (2023)
?
Surface conditions
Water collecting roof
Box 1
Box 2
Weekly water sampling
- Electrical conductivity
- Fluorescence test
Location: Tnl; Elev; ...
Gallery
Box 1 and Box 2 in 2022 and 2023:
- Flow rate - 10 min timestep
- Electrical conductivity - 10 min timestep
- Water temperature - 10 min timestep
Box 1 only:
- Fluorimeter - 10 min timestep in 2022
1 min timestep in 2023
Water measurements

182

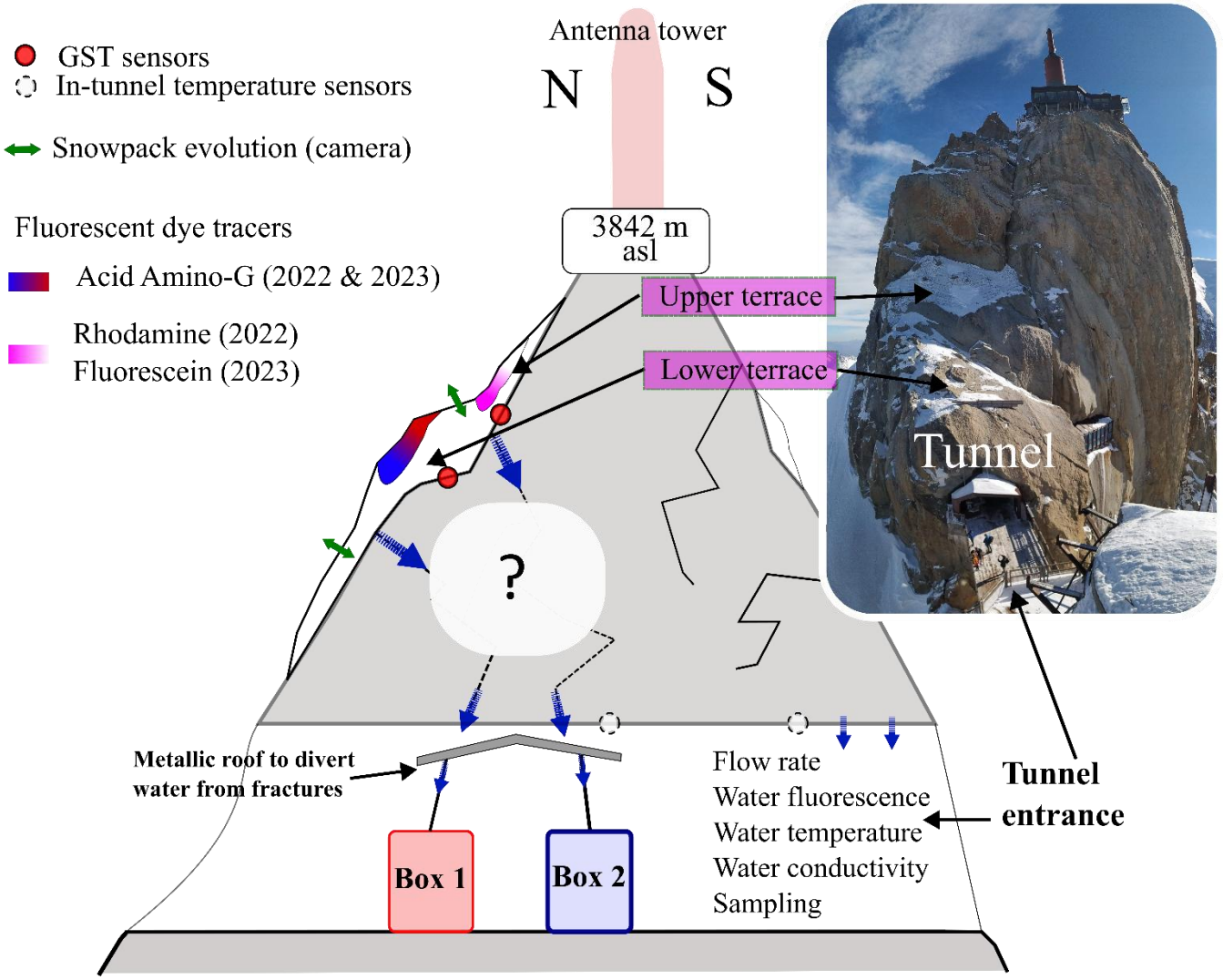

Figure 3: Sketch of the methodological approach to track and monitor water flows in the Aiguille du Midi central pillar. Note the location of the insertion of the dye tracers in the snowpacks on the terraces above the water monitoring boxes.

3.1. Fluorescent dyes in the snowpack

Fluorescent dyes were inserted into the snowpack at the surface above the ~~gallery~~tunnel in two locations, directly above the fractures ~~(5-15 m),~~(Figure 3), to trace the water source and rate of infiltration. In the 2022 season, two dye solutions were used: 20 L of sulphorhodamine-B solution with a concentration of 0.001 g/L and 20 L of amino acid G with a concentration of 20 g/L. ~~The~~These solutions were prepared and carried in "Ondine®" mineral water bottles ~~with~~by inserting the dye powders directly into the original mineral water, each with a volume of 5 L. The relatively low concentration of sulphorhodamine-B was chosen to have a light but detectable pink color, far above the detection limit of the fluorimeter sensor.

In 2023, new ~~concentrations~~solutions were prepared ~~for both tracers, and sulphorhodamine~~in the same manner, using 1.5 L bottles of "Ondine®" mineral water. Sulphorhodamine-B was replaced by fluorescein dye, a much more soluble and detectable dye, to avoid confusion with sulphorhodamine-B from the previous year.

~~Four bottles of 4 L and six bottles of 1.5 L of "Ondine®" mineral water were used to prepare the tracers solutions. The dyes in powder have been inserted directly into the bottles with the original mineral water.~~In total, 9 L of fluorescein solution with a concentration of 0.667 g/L and 16 L of amino acid G with a concentration of 12.5 g/L were prepared.

In both years of the study, tracers were injected into the snowpack at the same two locations on the north face of the central peak (Figure 3). Sulphorhodamine-B in 2022 and Fluorescein in 2023 were injected on the "upper" terrace of the face, which is located 18-24 meters above the tunnel, while amino acid G was injected on the "lower" terrace, 7-12 meters above the tunnel, in 2022 and 2023. ~~Tracers~~The tracers were inserted in spring, before the flow started~~,~~: on the ~~11~~11 May 2022 and ~~22~~22 March 2023. We poured the solution in 5-10 points ~~in~~on each terrace and on the snowpack surface.

3.2. Ground surface temperature at the snow-rock interface

Four miniature temperature sensors (iButtons, Mouser®) have been installed in holes drilled 5 cm into the rock surface, at the snow-rock interface, ~~in~~on the ~~vicinity of~~terraces where the fluorescent ~~dye injection area~~dyes were injected. The holes ~~with~~containing the coin-sized sensors were filled with gray polymer clay to ~~isolate~~insulate the metal sensors from direct solar radiation ~~on the metal sensor. They~~. The sensors monitored GST at hourly time steps and over different periods (~~Table 1),~~Table 1Table), but only one (#~~6202~~61B8) monitored the temperatures during both seasons.

Sensor ID	Monitoring period covered	Location on the face
7077	11/05/2022 to 23/09/2022	In drilled hole at base of vertical rock outcrop
6202	~~11/05~~06/09/2022 to 22/08/2023	In drilled hole at the surface of the lower terrace
608D	~~06/09~~11/05/2022 to 22/08/2023	In a hole drilled at the base of a rock outcrop above the lower terrace
61B8	~~23~~22/09/2022 to 22/08/2023	In the rock crack (same rock as 608D)

Table ~~1~~1: Miniature temperature ~~sensor characteristics~~sensors ('iButtons') at the snow-rock interface

Snow melting was ~~detected~~identified as "zero-curtain" periods in GST (Figure 5). These periods are characterized by stagnant GST at ~0 °C ~~(Hanson and Hoelzel, 2004).~~(Hanson and Hoelzle, 2004; Staub and Delaloye, 2017). The complete melting of the snow is marked by the transition from dampened GST daily oscillations to positive and significant daily oscillations ~~marks~~ once the insulating snow layer ~~of the snow is removed~~has melted and solar radiation reaches the rock surface. As GST is measured at point-scale ~~measurements~~, it lacks spatial representativeness of the snow melting surface area. Thus, to complete this data, pictures were frequently taken during fieldwork in 2022 to document snow patch evolution ~~in 2022, and in~~. In 2023, an automatic camera was installed (Figure 5) on a terrace of the North Pillar (~~North Camera~~See location on ~~Figure). It took 4 pictures a day from~~Figure 1). From 1 March 2023 to 22 August 2023, it took 4 pictures a day of the north face of the Central

Pillar, to monitor the snow patch evolution right above the water collection system. Pictures after 22 August 2023 are not usable because the protective glass was broken, and the pictures became blurred.

3.3. Water flows and temperature monitoring in the ~~gallery~~tunnel

We installed a real-time monitoring system in May 2022 in the west ~~gallery~~tunnel of the Central Pillar, to characterize the water flowing from fractures that cross the ~~gallery~~tunnel walls. We took advantage of an existing water diversion ceiling set up by the operating company (Figure 4), made of a convex metallic plate ~~collecting~~that collects water drips and flows, and ~~diverting~~diverts them to two pipes, one on each side of the ~~gallery~~tunnel (east and west) to drain water outside. Preliminary observations revealed that water was mostly dripping from two adjacent fracture systems~~.~~ with a generally subvertical dip (70°-90°) oriented toward north-west.

~~Instrumentation~~The instrumentation included two rain gauges that were installed on each pipe to measure water flow rate (L/h), in protective boxes (Box 1 on the west side and Box 2 on the east side). Water temperature (°C) and electrical conductivity (S/cm) were also monitored with sensors placed on the metallic roof, below the identified water drips. The sensors were ~~plunged~~submerged in a specially designed ~~and~~, 3D printed, siphon~~-~~-shaped pipe (Figure 4B) to maintain a high water exchange rate and a minimal water level for detection. As a conductivity benchmark, we measured a value of 9.2 µS/cm from a melted snow sample collected on the ~~26th of~~26 July 2023 ~~and~~, which corresponds with known values for snowmelt samples (Brennan et al., 2020; Thompson et al., 2016). In addition, water fluorescence (arbitrary units) was monitored in real-time with a probe ~~(GGUN-FL-24)~~ inserted in Box 1 to detect the specific emission spectrum of the dye tracer used: ~~Acid~~ Amino-acid-G and sulphorhodamine-B in 2022 and Amino-acid-G and Fluorescein in 2023 (see Sect. ~~3.2~~3.1 for dye spraying strategy). The fluorescence sensor installed in 2022 (GGUN FL-24) malfunctioned during the 2022 winter and was replaced by a new probe (STREAM model, TRAQUA®) on the ~~31st of~~31 May 2023, and was removed on the 22nd of August several weeks after the last dye signal was detected.

~~Every 10 minutes, five measurements~~Average values from the installed sensors were ~~averaged and~~ recorded every 10 minutes with a PC400 Campbell Scientific data logger. In addition, data from miniature temperature sensors (iButtons, Mouser®) that were previously installed~~,~~ were used to monitor the ~~gallery~~tunnel wall (bedrock) temperature.

The site was visited weekly ~~to retrieve data and to clean the rain gauge where sediments were sometimes accumulating (Figure 4).~~

~~In 2023 the conductivity sensor was fixed directly below fracture, above box 1, during the thawing season, .~~excluding a short period from 25 July 2023 to 10 August 2023 because of a storm~~. In addition,~~ that prevented access, to retrieve data, take water samples and manual measurements on electrical conductivity ~~was also measured manually directly in water samples in Box 1, using a mobile sensor, once a week.~~, and to clean the rain gauge, since sediments sometimes accumulated (Figure 4).

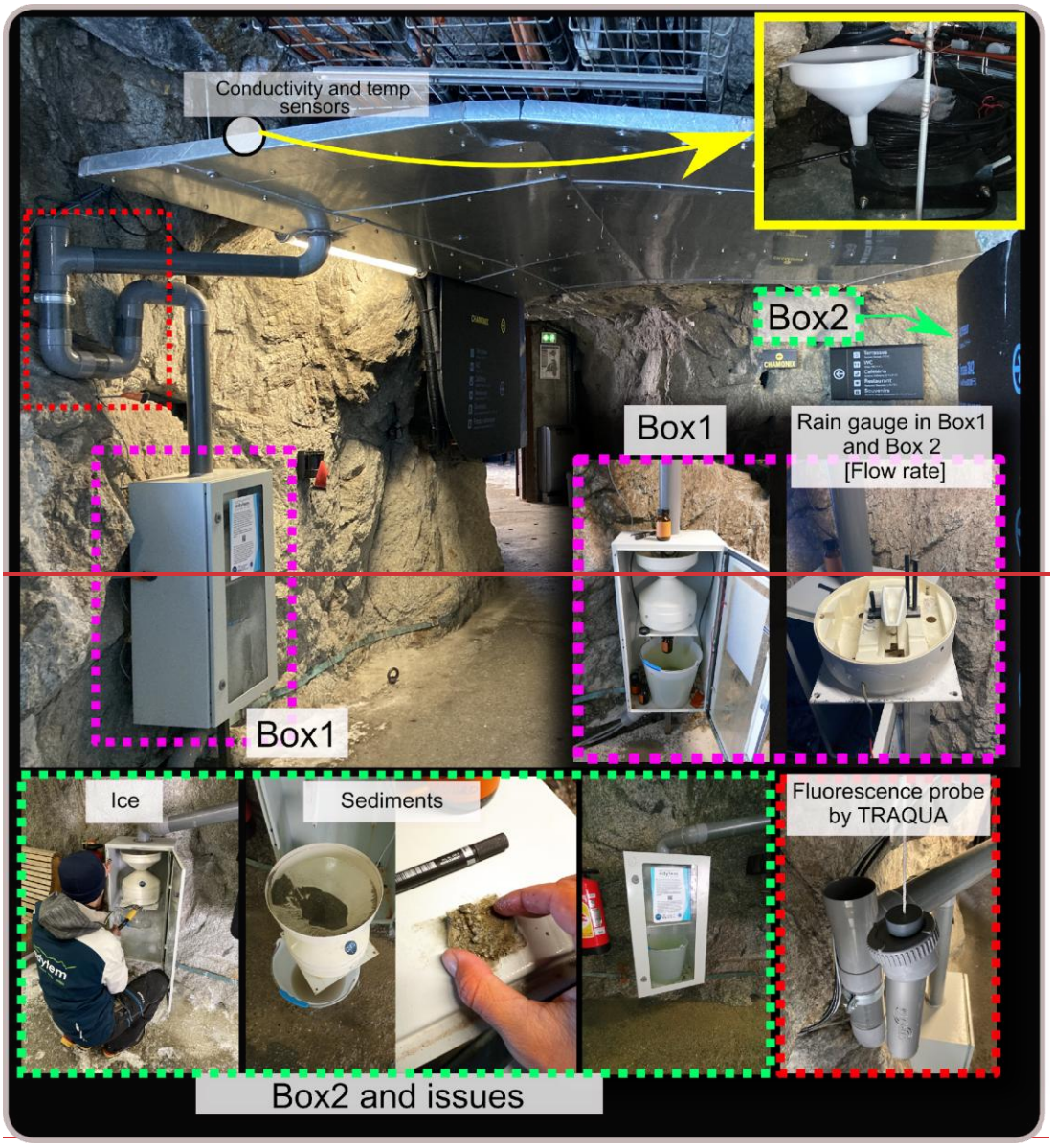
Conductivity and temp sensors
Box2
Box1
Rain gauge in Box1 and Box 2 [Flow rate]
Box1
Ice
Sediments
Fluorescence probe by TRAQUA
Box2 and issues

250

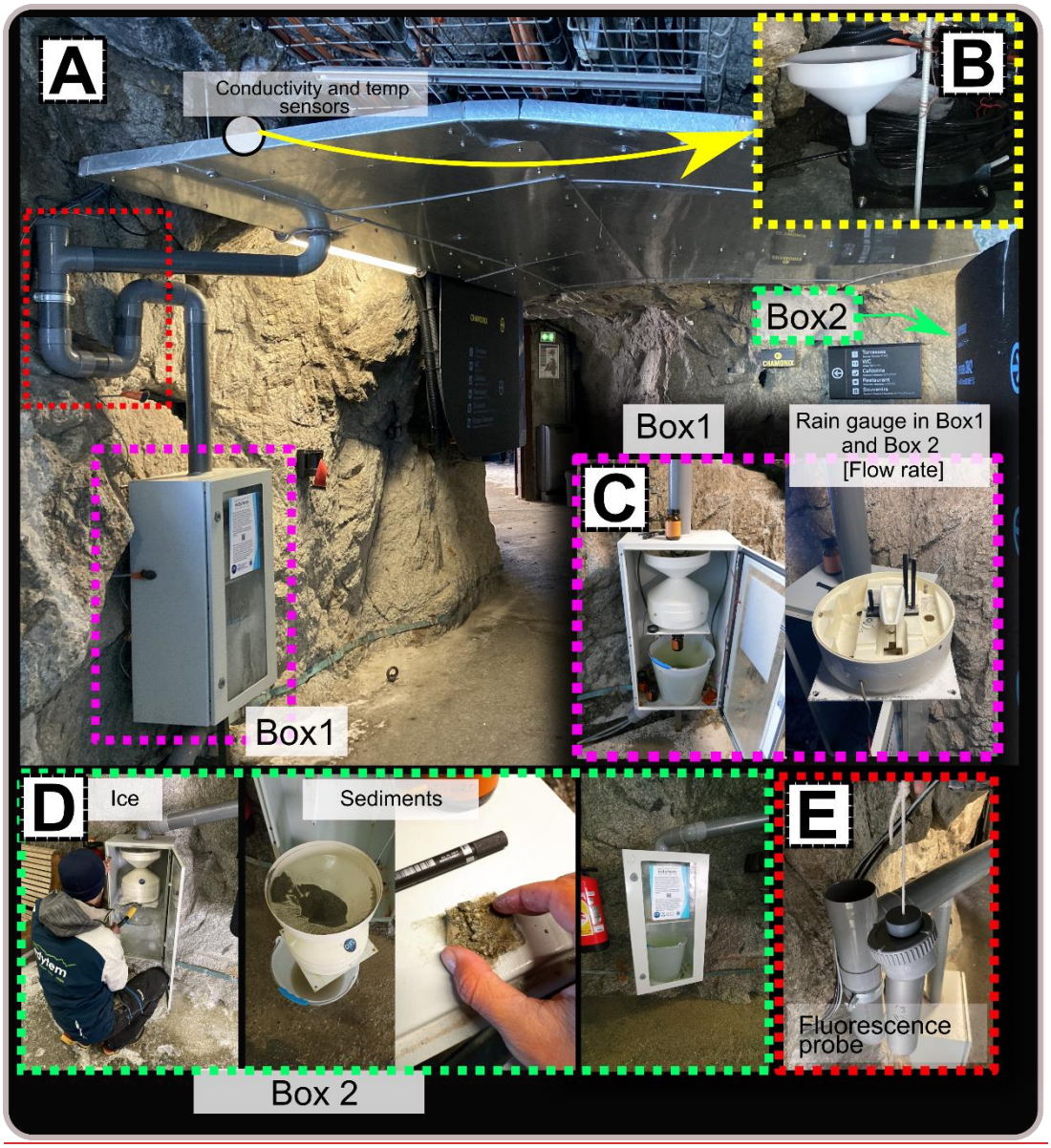

Figure 4: Real-time monitoring system in the ~~gallery, including Box 1 and 2 with the flow gauge (purple~~tunnel. A) The metal roof and Box 1 (pink dashed frame~~),~~). B) A 3D printed siphon ~~with fluorescence probe (red~~that was placed directly under the water output from the fracture, equipped with temperature and conductivity sensors (yellow dashed frame). ~~Images of~~ C) Box 1 interior with rain gauge to monitor flow rate, a sampling bottle, and a bucket. D) Box 2 with sediments ~~are shown in the~~ (green dashed frame~~.~~). E) Fluorescence probe by TRAQUA located in a specially designed siphon for continuous real-time monitoring of the dye tracers.

3.4. ~~—~~Water sampling in the ~~galleries~~tunnels and laboratory analysis

Water samples were collected weekly from Box 1 during the melting seasons of both 2022 and 2023~~ melting seasons.~~. Other locations in the ~~gallery~~tunnel (labeled Box 2~~,~~ and TNL) were sampled occasionally ~~sampled~~ in 2022 and weekly in 2023. Samples were taken in 125 mL brown glass bottles. During the 2023 season, the electrical conductivity of each sample was measured ~~for electrical conductivity,~~ directly after collection. The bottles were stored in a fridge~~, protected from light~~ to minimize biological activity and protect them from light.

Further high-resolution fluorescence analysis of the water samples was carried out in a laboratory, using a fluorescence spectrophotometer (Varian Cary Eclipse) to validate the real-time fluorimeter data. The samples were exposed to light ~~with the characteristic~~whose wavelength spectrum ~~matching~~matched the excitation spectrum of the dye tracers used in the experiment. The emission vs. excitation wavelength plots were used to find peaks in emission distribution that corresponded to the presence of the dye tracers.

In addition to fluorescence analysis, we performed stable isotope analysis on 11 water samples to determine $\delta^{18}O$ and δD values. ~~These stable~~Stable isotopes are widely used in hydrological studies to trace the origin and history of water, as their ratios are sensitive to fractionation during phase changes in the ~~hydrologic~~hydrological cycle. Such analyses can reveal important information about water sources (e.g. snowmelt vs. rainfall), transport pathways, and storage times. By comparing the measured isotopic signatures to the Global Meteoric Water Line (GMWL), we can assess whether the water follows typical meteoric patterns or has undergone secondary processes such as evaporation, mixing, or prolonged subsurface residence. Deviations from the GMWL can also indicate elevation effects or seasonal variations in precipitation, making isotope data a valuable complement to physical and chemical tracers in characterizing alpine hydrological systems.

3.5. Data analysis

~~3.6.~~ We processed and analyzed the continuous time series data by developing codes in Python3 and MATLAB. All ~~the~~ time series were filtered for erroneous values and interpolated to evenly spaced time steps for consistency.

~~3.6.1.~~3.5.1. Recession curves analysis

Recession curves have been studied since the late 19th century (Brutsaert and Nieber, 1977; Tallaksen, 1995) and are commonly used in hydrology to interpret the flow behavior and characteristics of aquifers. A key advantage of this approach is that it allows the derivation of empirical, quantitative parameters that reflect the subsurface drainage. Following work by Boussinesq (1877), Maillet (1905) suggested an exponential analytical solution to describe aquifer drainage behavior:

$$Q(t) = Q_0 e^{-at} \quad (1)$$

where Q is flow rate, t is time, Q_0 is peak flow rate, and α is the recession coefficient. To account for flood recession in a channelized flow, we opted for the general form suggested by Brutsaert and Nieber (1977) that is commonly used for river flood recessions (Brutsaert and Nieber, 1977; Krakauer and Temimi, 2011):

$$\frac{dQ}{dt} = -aQ^b \qquad (2)$$

which can be integrated and solved for $Q(t)$ as:

$$Q(t) = (Q_0^{1-b} - a(1-b)t)^{\frac{1}{1-b}} \qquad (3)$$

where a and b are constant coefficients. Note that the integration of Equation 2 in the case of $b=1$ corresponds to the form of exponential decay as expressed by Equation 1. Scandroglio et al. (2025) recently applied Maillet's law (Equation 1) to analyze flow in fractures within a permafrost-affected rock wall in the Northern Calcareous Alps, at the German-Austrian border. ~~Their study focused on a 55 m deep tunnel in karst limestones, where flow paths could extend for several hundred meters. In contrast, in our study, flow is confined to widely open, sub-vertical granite fractures with a maximum path length of 30 meters. Additionally, Scandroglio et al. (2025) used a single best-fit curve for their entire dataset, which included only 23 events over eight years. In comparison, we used 93 events for recession curve analysis (out of 144 events that were recorded, see 4.1.5 for more details) over two consecutive. To capture temporal variations in flow characteristics, we developed an algorithm that automatically fits a separate curve to individual events, allowing us to track changes over time and compare flow behavior between Box 1 and Box 2 (Figure S2).~~ Their study focused on a 55 m-deep tunnel in karst limestones, where flow paths extend at least 55 m and possibly farther due to tortuosity. In contrast, in our study, flow is confined to widely open, sub-vertical granite fractures with path lengths ranging from 12 m (lower terrace) to 20 m (upper terrace). Additionally, while we define a flow event as the period between a well-defined rise and the following recession of the hydrograph, Scandroglio et al. (2025) defined an event as a flow period beginning with a sudden increase in discharge, independent of the starting value, and ending when the flow returns below a set threshold, potentially including several peaks. They applied a single best-fit curve to their entire dataset, which comprised 23 such high-flow events over eight years. Their approach is well suited to rain-controlled conditions. In contrast, our field site at 3840 m a.s.l. is dominated by snowmelt and thus strongly influenced by the diurnal solar cycle. We therefore identified 93 well-defined single-peak events for recession-curve analysis over two consecutive seasons. To capture temporal variations in flow characteristics, we developed an automated algorithm that fits a separate recession curve to each event, enabling to track changes in flow behavior over time (Figure S2, S4). For each event, the algorithm identifies the recession limb as the interval between the last local maximum and the subsequent return to baseflow. It then isolates the concave segment of this limb (curvature > 0), which corresponds to the exponential decay, and fits the appropriate form of Eq. 1 or Eq. 2. To ensure that only well-defined exponential recessions are included, events with regression fits yielding $R^2 < 0.8$ are discarded. This threshold retains 64% of all detected events (93 out of 144) while excluding cases where noisy or multi-peak recession behavior prevents reliable fitting.

~~3.6.2.~~3.5.2. Moving window cross-correlation

A moving ~~-~~window cross-correlation analysis was ~~used~~performed to ~~estimate~~quantify the correlations and lag times between ~~measurement~~pairs of measured time series~~. All the ~~, including flow rate, AT, and GST. For each lag time, the Pearson correlation coefficient (PCC) was calculated between one series and a time-shifted version of the other (+1: high correlation, 0: no correlation, -1: reverse correlation). For example, at a lag time of 0, the flow and AT were measured at the same time; at a lag time of +6 h, the flow series was correlated with the AT series shifted forward by 6 h . Lag times were evaluated in the range of –12 to +12 h in steps of 1 h.

The analysis was performed in a moving window of 24 hours starting from 00:00, without overlapping, which corresponds to the observed daily cycles in both flow rate hydrograph, and GST and AT. Window size is an important parameter: shorter windows highlight transient events but may be sensitive to noise, whereas longer windows yield more stable estimates at the cost of smoothing short-term variability. In this study, a window length of 24 hours was selected as a compromise between detail and stability.

Prior to analysis, all time series were filtered with a ~~high pass~~one-hour moving ~~-~~ average ~~filter of one hour~~ to reduce high-frequency noise. ~~Cross-correlation analysis was carried out on~~Only days ~~when the~~with a maximum flow rate ~~exceeded~~above 6 L~~/~~ h~~. This value was chosen as a threshold to filter data from days~~$^{-1}$ were included, ensuring hydrographs with ~~well-defined hydrograph curves. These include data from 109.~~clear diurnal signals. The analysis was ~~made on~~conducted over the entire ~~period of observed water~~ flow ~~in each~~ season~~, i.e.~~ (mid-May to August in 2022, and June to September in 2023~~.–~~).

4. Results

4.1. Water flow rate

~~4.1.1. Seasonal pattern~~

Water flow is highly seasonal. In both years, water mostly flowed between May and October ~~(Figure 5),~~ with periods of sporadic and continuous flow that can last several weeks. The occurrence of water flows correlates with the occurrence of positive AT (Figure 5).

~~Sustained~~In 2022, sustained periods of water flow were mainly observed from late May to mid-September ~~in 2022~~, and in 2023, from mid-June to late September ~~in 2023~~. The timing and magnitude of the flow differed between Box 1 and Box 2 (~~Figure 6).~~Figure 6). In both years, water flow in Box 1 ~~started~~began several weeks ~~before that~~earlier than in Box 2. In general, the amount of water in Box 2 increased ~~through~~throughout the summer season.

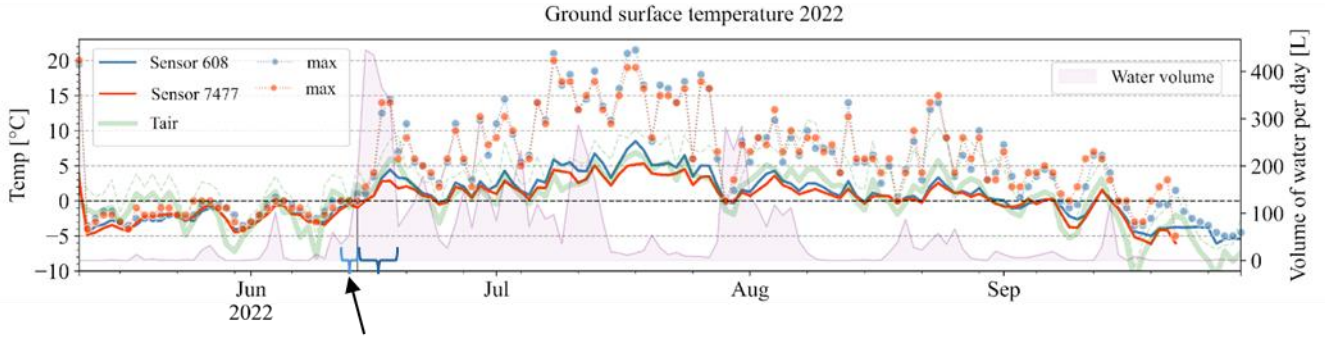

zero-curtain period followed by a high flow rate

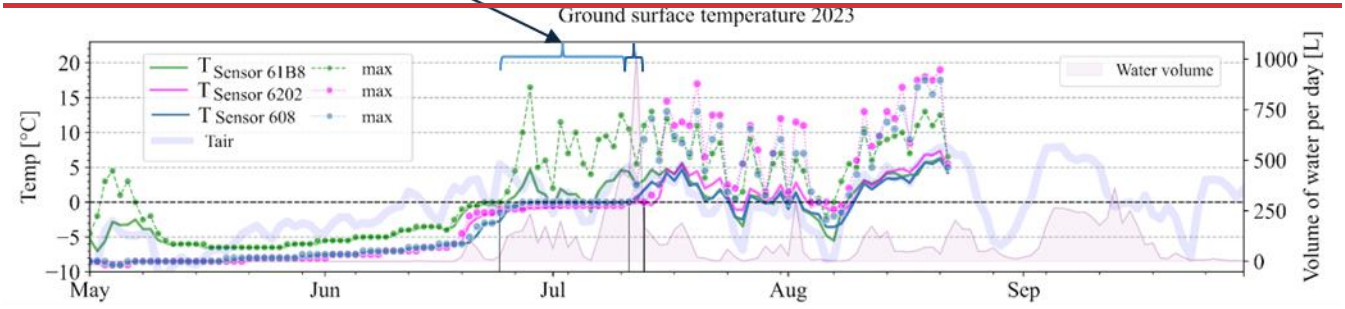

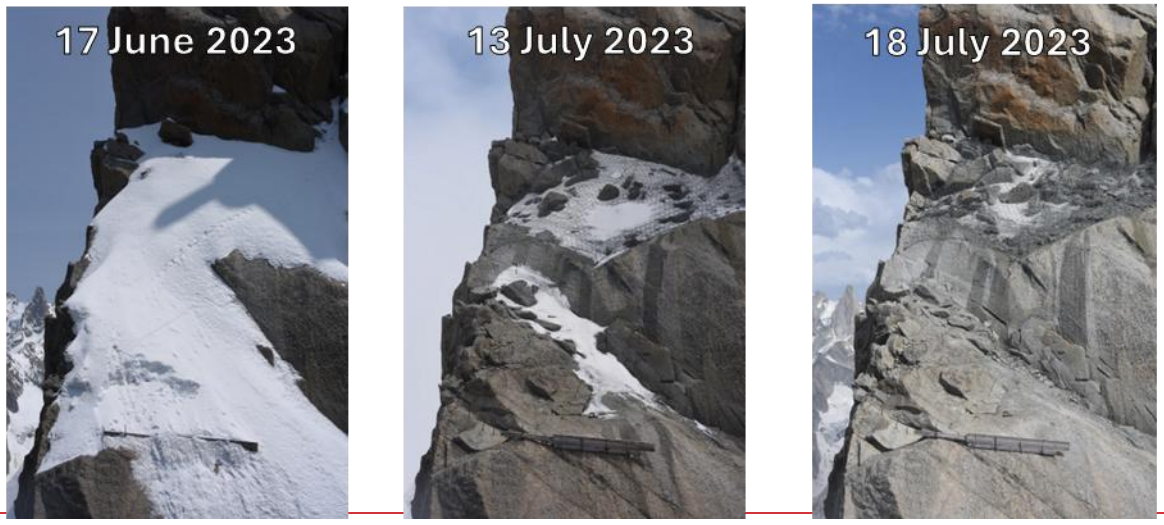

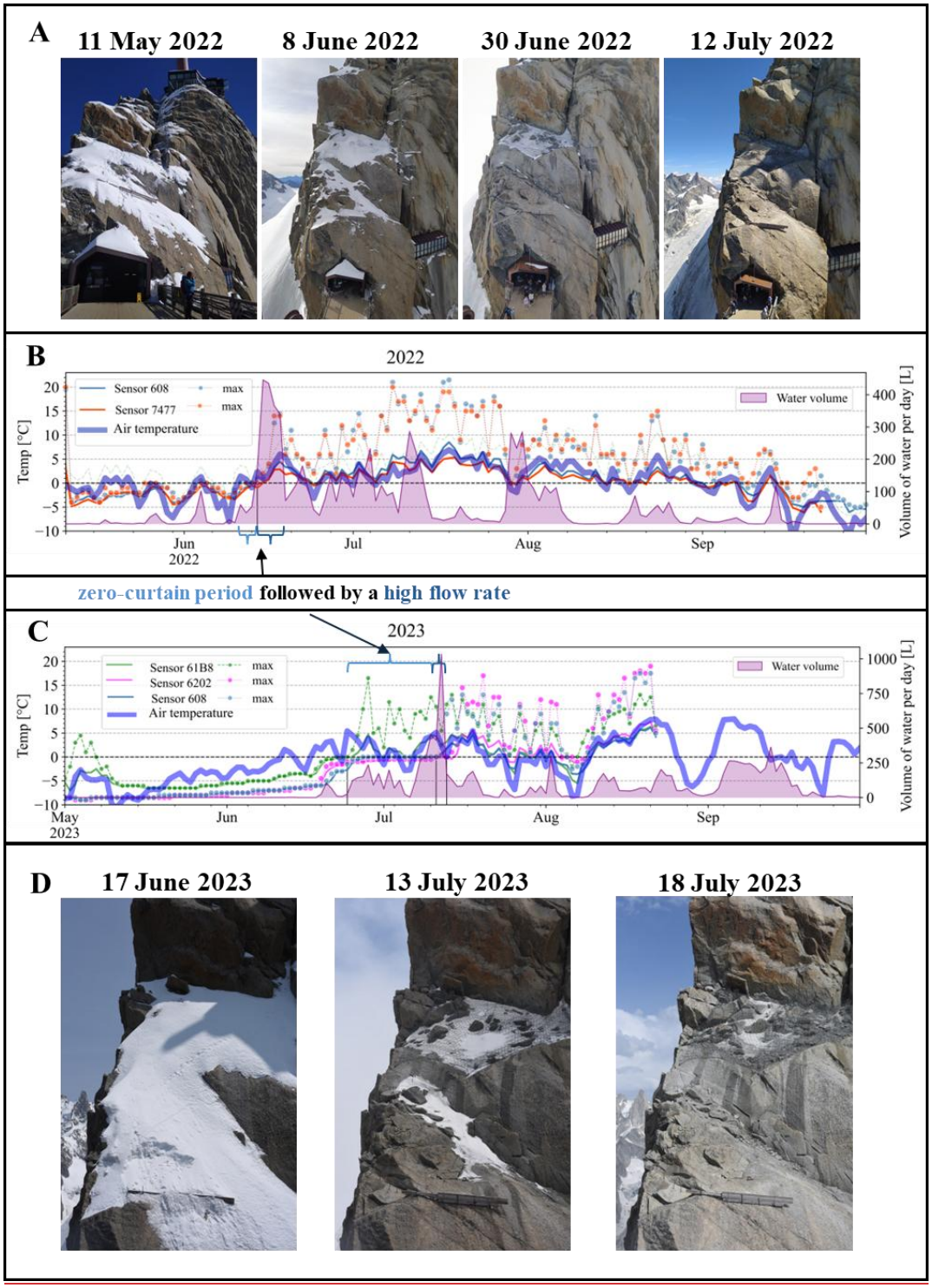

Figure 5: A) Photos showing the evolution of the snow cover on the NE face during the snow melt season in 2022. B) and C) AT, GST ~~are~~ measured on the NE face, above the ~~gallery~~tunnel entrance, directly above the monitoring system~~. Flow~~, and flow rate ~~is~~

measured at the output from rock fractures in the ~~gallery~~tunnel wall~~.~~ (Box 1+Box 2) in 2022 and 2023, respectively. Solid lines represent the daily ~~mean~~average. Note the zero-curtain period, which marks the ~~thawing~~melting of the snowpack and the exposure of the rock surface to atmospheric heating. D) Photos showing the evolution of the snow cover on the NE face during the ~~thawings~~now melt season in 2023.

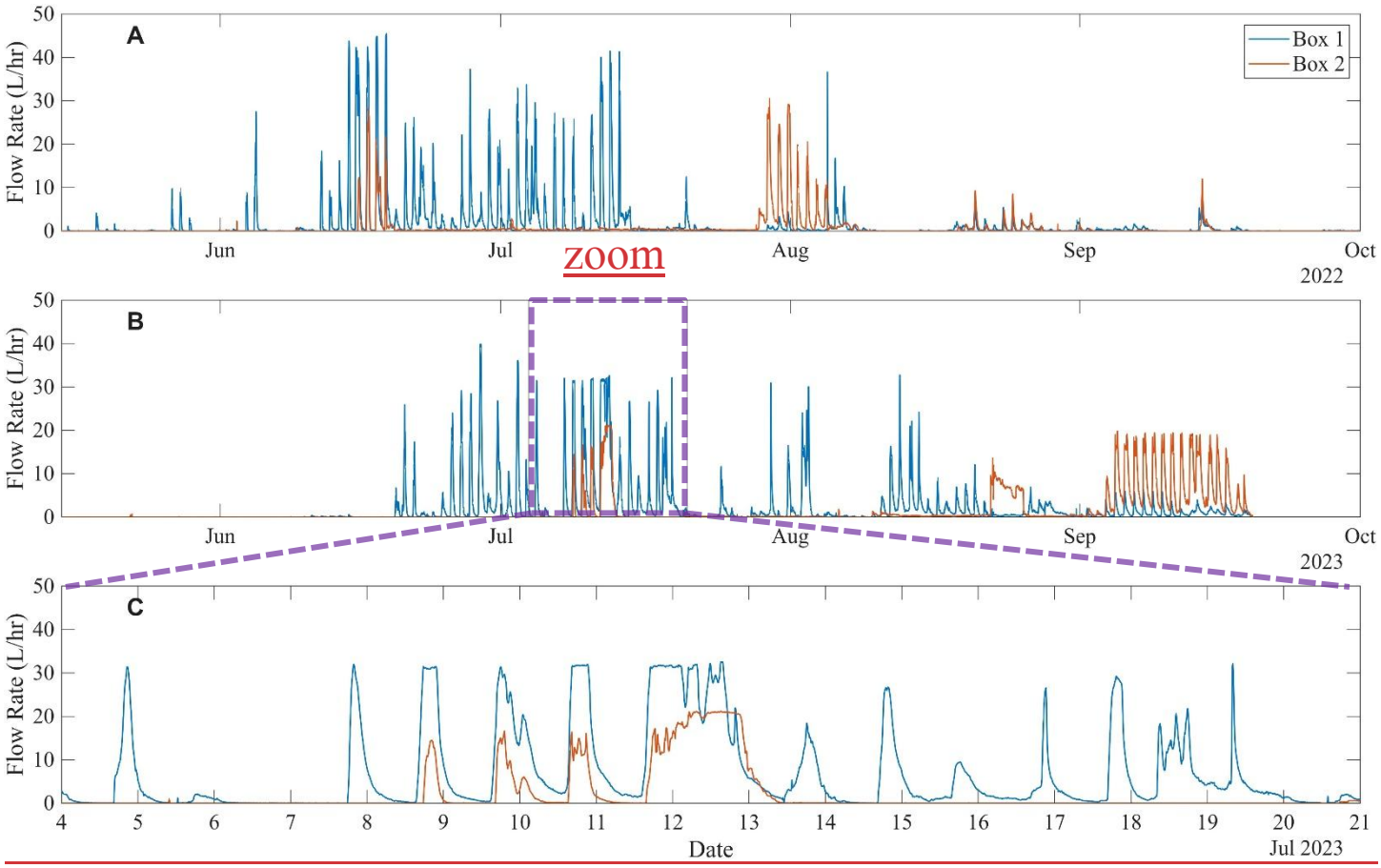

Figure 6: A) and B) Time series of flow rate in Box 1 (blue) and Box 2 (orange) during the 2022 and 2023 melt seasons ~~in 2022 and 2023~~, respectively. C) Zoom window on the 4-21 July 2023 period.

In 2022, the total volume of water flowing through the monitoring system (~~Box~~Boxes 1 and ~~Box~~ 2) was 8001 L ~~(Figure 6).~~ About 70% of this ~~total~~ volume (5621 L) was collected in Box 1, while ~~about~~the remaining 30% (2380 L) reached Box 2 ~~(2380 L).~~. 75% of the total volume in Box 1 occurred between ~~the 11th of~~11 June and ~~the 14th of~~14 July (4216 L). ~~From~~Of the total flow volume in Box 2, 74% flowed in two relatively short periods: ~~between the 14th 19th of~~14 - 19 June (496 L) and ~~between the 28th of~~28 July ~~and the 8th of~~ 8 August (1257 L).

In 2023, the total volume of water flow was 11605 L ~~-~~ 45% more than in 2022~~, of which~~. Of this, 61% (7079 L) flowed through Box 1, and 39% (4526 L) in Box 2. 75% of the total volume in Box 1 occurred between ~~the 19th of~~19 June and ~~the 10th of~~10 August (5309 L). In Box 2, almost the entire volume (95%) flowed in three relatively short periods (3 to 18 days):

~~between the 8th - 13th of~~ 8 - 13 July (831 L), ~~between the 22nd - 25th of~~ 22 - 25 August (611 L) and ~~between the 1st - 18th of~~ 1 - 18 September (2851 L).

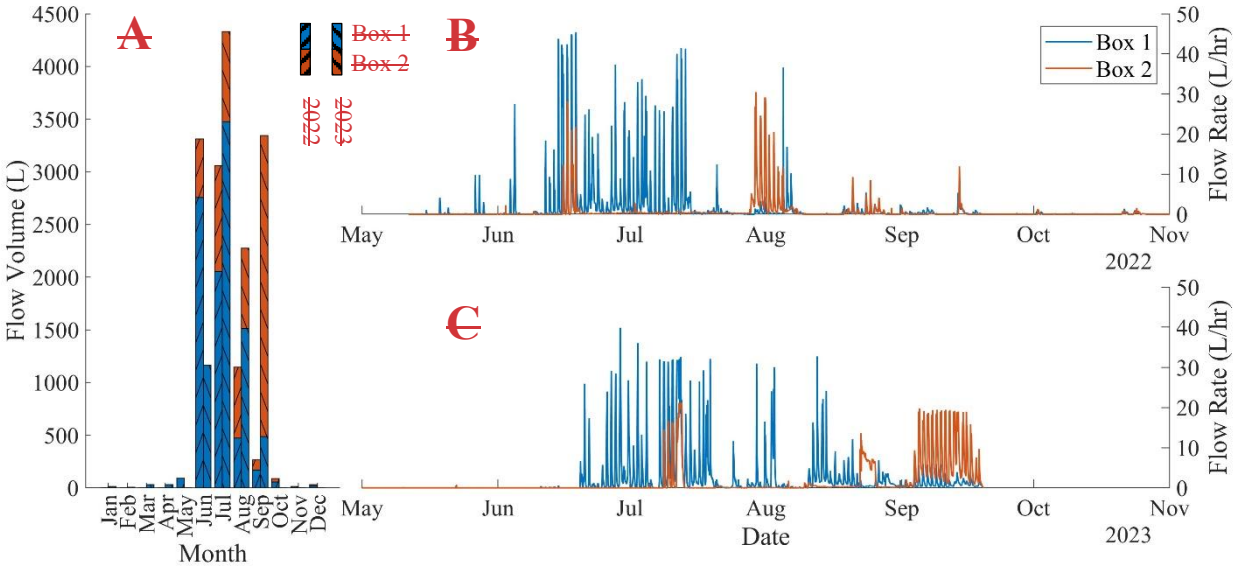
A
B
C
Box 1
Box 2
2022
2023
Flow Volume (L)
Flow Rate (L/hr)
Month
Date
Jan
Feb
Mar
Apr
May
Jun
Jul
Aug
Sep
Oct
Nov
Dec
2022
2023

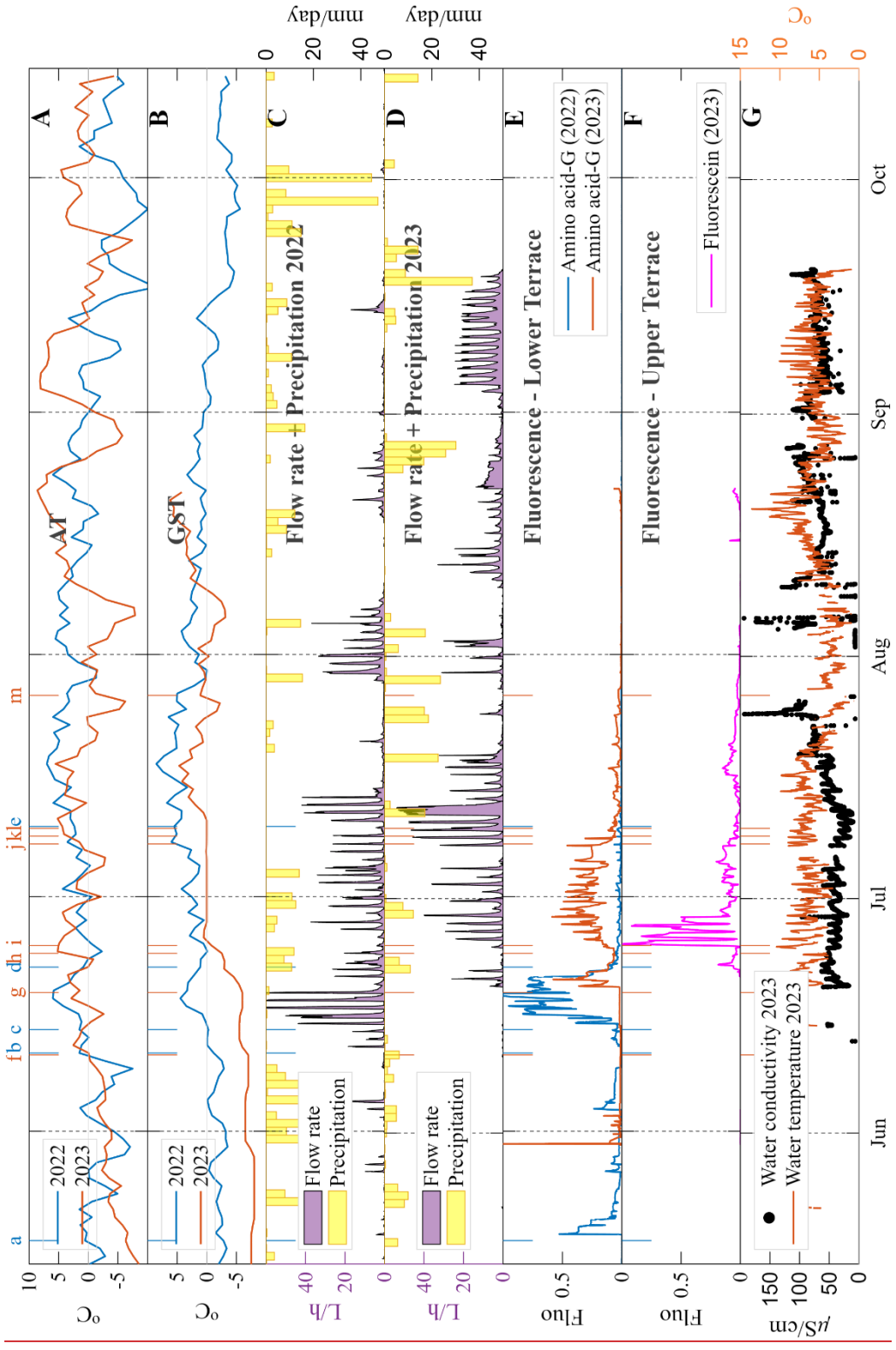
A
B
C
D
E
F
G
AT
GST
Flow rate + Precipitation 2022
Flow rate + Precipitation 2023
Fluorescence - Lower Terrace
Fluorescence - Upper Terrace
2022
2023
Flow rate
Precipitation
Amino acid-G (2022)
Amino acid-G (2023)
Fluorescein (2023)
Water conductivity 2023
Water temperature 2023
°C
L/h
mm/day
Flu
µS/cm
Jun
Jul
Aug
Sep
Oct

367

Figure 7~~: Water flow rate distribution in both boxes~~

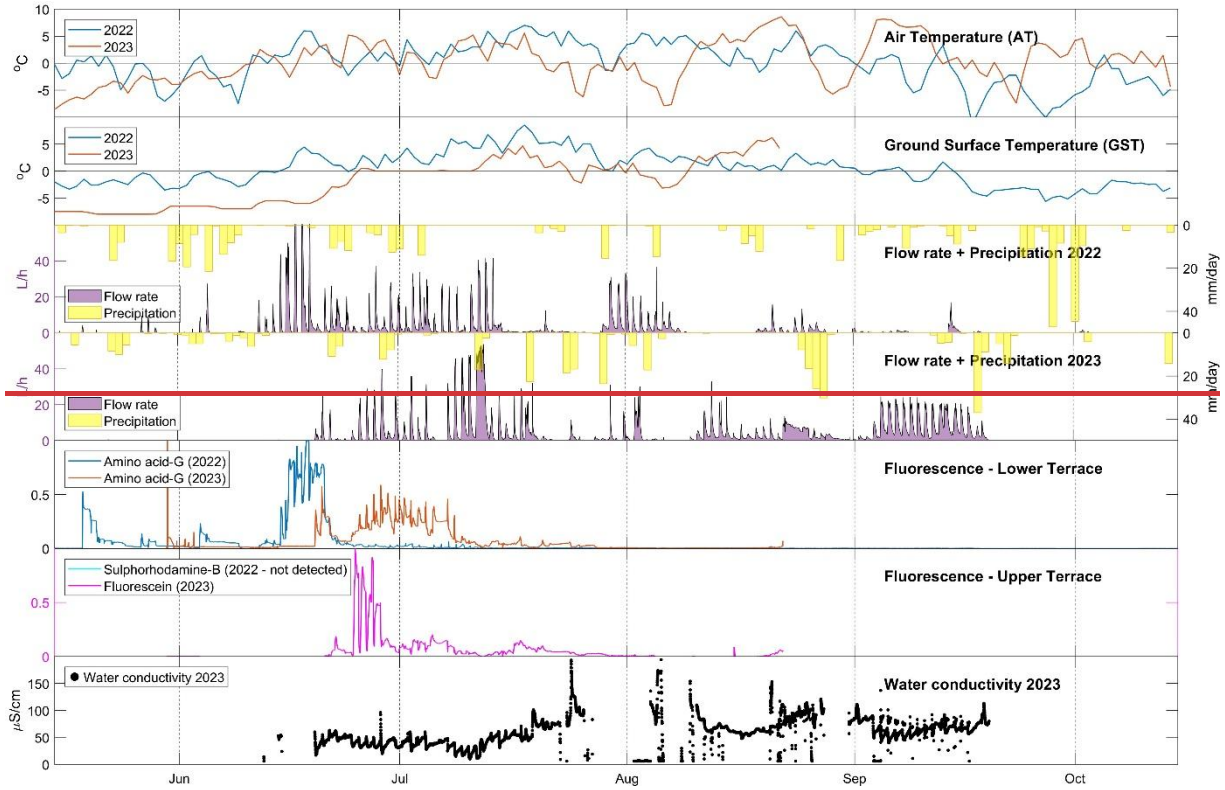

~~Figure 7: Annual time series~~

~~4.1.2. Daily patterns and flow rates~~

~~: Annual time series. A) Air temperature (AT) measured by Météo-France in Aiguille du Midi. B) Ground surface temperatures (GST) measured using iButtons at the rock surface on rock slope. C-D) Flow rate measured in both box 1 + box 2 (purple) and daily precipitation measured in Chamonix meteorolocical station (Météo-France) (yellow bars). E) Normalized fluorescence signal of amino acid-G dye tracer (2022 and 2023). F) Normalized fluorescence signal of Sulphorhodamins-B (inserted in 2022) and Fluorescein (inserted in 2023) dye tracers. The Sulphorhodamins-B dye was never detected. G) Water conductivity and temperature at the outlet of water from the fracture in the tunnel. Measurements in time steps without water flow were omitted from the plot. Labeled annotation at the top of panel A mark the following main events in 2022 (blue): a) first flow event in box 1, b) AT surpasses 0° C, c) GST surpasses 0° C + beginning of daily oscillations + first flow in box 2, d) amino acid G signal diminishes, e) last amino acid G signal, and 2023 (orange): f) AT surpasses 0° C, g) first water flow event in box 1, h) beginning of daily oscillations, i) beginning of zero curtain, j) first flow in box 2, k) amino acid G signal diminishes, l) end of zero curtain, m) last amino acid G signal.~~

The observed flow rate presents daily cycles (~~Figure 7~~Figure 6) with peak flow rates, reaching an order of 10^1 L/h, generally occurring between 17:00 to 20:00 (~~Table 2~~Table 2, Figure S1), and minimum flow rates two orders of magnitude lower (order of 10^{-1} L/h) during the morning time.

	Average time of signal peak	
	2022	**2023**
Air temperature (AT)	~~11:40~~12:00-15:00	11:~~30~~00-15:00

Ground surface temperature (GST)	~~15~~15:30-18:00	~~14~~15:30-17:00
Flow rate	:18~~40~~00-19:50	~~18~~16:20-20:30

~~**Table 2: Average timing and lag time of flow peak and AT.**~~

Table 2: Time of day of the daily peak in flow rate, AT, and GST. The listed time ranges represent the 25–75% quantile of daily peak timing

Results of a moving window cross-correlation show that daily flow rate oscillations are correlated with AT ~~measurements~~ with a lag time of 3-9 hours, and with GST with a lag time of 0-~~3~~6 hours. This lag time was found to be ~~consistent~~steady in both years of the experiment (Table 2, ~~Figure S3).~~Figure 8).

~~4.1.3. 2022 season~~

~~In 2022, the first flow event was recorded in the system in Box 1 on 15 May 2022 around 17:00 and reached a maximum flux of 1.1 L/h (Figure 7). Sporadic daily events continued to occur in Box 1 with a general trend of increasing flow rate (reaching 9.9 L/h) until the 11th of June. From that date, a 5-week period of continuous flow started in concomitance with positive AT, and daily cycles sometimes reaching rates of > 40 L/h. The continuous water flow period ended on the 14 July 2022, although the AT was still positive and even reached its maximum value, likely indicating the complete thawing of the winter snowpack. The water flow events that followed and recorded in Box 1 are linked to precipitation that most likely fell as rain since the AT was positive (Figure 5, Figure 7). In Box 2, the first flow event occurred early in June, with the first significant event (> 10 L/h) on 15 June 2022, when the AT increased, and after a short period of low flow rates. This event was followed by 5 days of continuous flow with daily oscillations reaching > 25 L/h, similar to those observed in Box 1 at that period, but starting 5 days later (Figure 7). A period of low flow rates continued in Box 2 until the 28th of July when an 8-day period of high daily flow rate reaching up to 30 L/h with strong daily oscillations started with a precipitation episode, two weeks after the end of the high flow rate period in Box 1. A few low flow rate events still occurred between October and December.~~

~~The maximum flow rate recorded was 45.4 L/h in Box 1 (18th of June 2022 at 18:40), and 30.46 L/h in Box 2 (29th of July 2022 at 18:50). Cumulating flows from Box 1 and Box 2, the maximum flow rate was 67.35 L/h with 39.42 L/h in Box 1 and 27.96 L/h in Box 2 the 16th of June 2022 at 19:20. The maximum daily amount was 445.9 L on the 15th of June 2022.~~

~~4.1.4. 2023 season~~

~~In 2023, the first flow started with a significant oscillation on 19 June 2023 in Box 1, that was the onset of continuous daily oscillations, with an increasing trend in maximum daily flow rate reaching 40 L/h on 28 June 2023. The flow rate then decreased with to maximum daily values < 10 L/h, and a whole day without flow occurred on the 6 July 2023. This interruption in daily oscillations coincides with a short-term decrease of AT below 0°C. From the 20 July 2023 to the 10 August 2023, daily oscillations were more sporadic, in lagged correlation with AT oscillations, water flow occurring under positive AT and~~

no flow under negative AT. The largest daily oscillations during this period, sometimes reaching up to 30 L/h, are linked to precipitation episodes with ATs sometimes close to 0 °C, hinting at possible rain events (Figure 5, Figure 7). From the 11 to 22 August 2023, continuous daily oscillations occurred again as the AT reached its maximum of the year and were stopped by a decrease in AT coinciding with an intense precipitation episode (reaching up to > 35 mm/d). A final flow phase occurred in Box 1 in September, with regular daily oscillations but rather low rates (around 5 L/h).

Box 2 experienced its first daily oscillations between the 8th and 13th of July, after about 3 weeks of generally positive AT, but with maximum daily oscillations remaining below those of Box 1 (up to 20 L/h against 30 L/h). A second water flow episode occurred between the 22nd and the 25th of August. This event was unusual because it lasted for 3 days without the characteristic daily recession but continued steadily at a flow rate of 5–12 L/h between the morning of the 22nd to the night of the 25th of August. This event is also enigmatic because it occurred after two weeks without precipitation documented in Chamonix and relatively high temperatures, during which Box 1 flowed regularly. It was followed by a 9-day period without flow. Final flow phase with regular daily oscillations occurred between the 3rd and 19th of September, and with maximum flow rates of 20 L/h, that is 4 times higher than in Box 1 during the same period. This important water flow episode occurred with the onset of positive AT, following a several days period of temperature drop below 0 °C and precipitation episode that likely occurred as snow.

There was also an exceptional one-off event between 11 and 13 July 2023, when, on both boxes, the flow continued for 2 full days after a precipitation event and during a short-term decrease in AT (despite still being positive).

In 2023, the maximum flow rate observed separately was 39.83 L/h in Box 1 on 28 June 2023 at 19:40, and 21.20 L/h in Box 2 on 12 July 2023 at 15:10. Cumulating flows from Box 1 and Box 2, the maximum flow rate observed was 53.81 L/h with 32.58 L/h in Box 1 and 21.18 L/h in Box 2 the 12 July 2023 at 15:10. The daily maximum volume was 1032.99 L on 1 July 2023.

~~4.1.5. Recession analysis~~

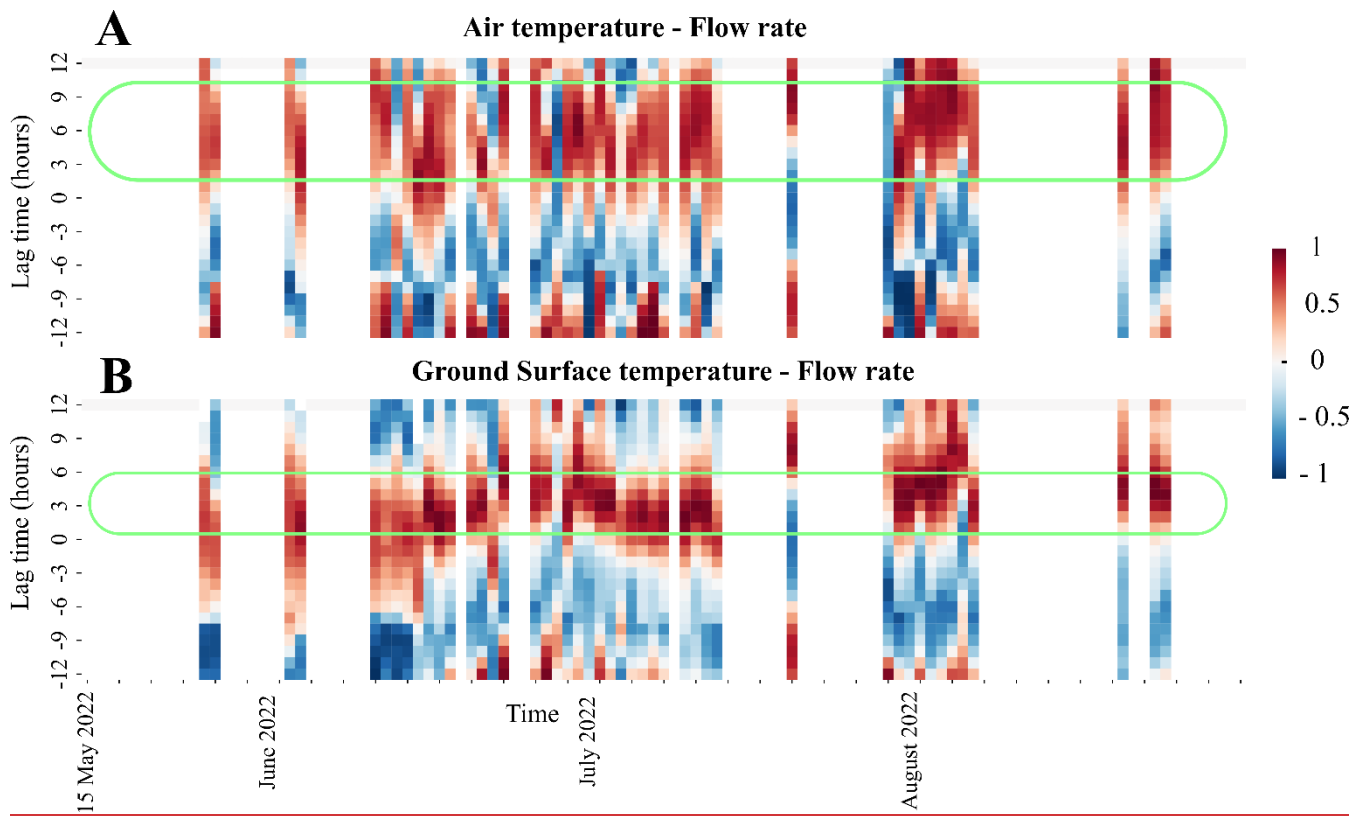

Figure 8: Results of moving-window cross-correlation analysis between the water flow rate and the (A) air temperature and (B) the ground surface temperature, during 2022 season. The horizontal axis represents the time (one strip per day), and the vertical axis represents the lag time, in hours. The color bar represents the value of the Pearson correlation coefficient (PCC) (1: high correlation, 0: no correlation, -1: reverse correlation). The green frame marks the range of lag times that show high PCC. Results of the cross-correlation analysis of 2023 season show similar results and can be found in the supplementary materials, in figure S3.

In 2022, the first flow in Box 1 was recorded on 15 May (1.1 L/h) and gradually increased, reaching continuous daily flows with peak values larger than 40 L/h from 11 June to 14 July, after which flows were linked to rainfall. Box 2 showed its first significant flow (>10 L/h) on 15 June, with continuous daily oscillations lagging about 5 days behind Box 1. Maximum flow rates were 45 L/h in Box 1 and 30 L/h in Box 2, with a combined peak of 67 L/h on 16 June.

In 2023, Box 1 exhibited continuous daily oscillations from 19 June, peaking at 40 L/h on 28 June, interrupted by short cold spells, and resuming under positive AT and precipitation events (Figure 6). Box 2 began daily flows between 8–13 July (up to 20 L/h) with a prolonged steady flow (5–12 L/h) from 22–25 August despite minimal precipitation. Maximum individual flows were 39.83 L/h in Box 1 and 21.20 L/h in Box 2, with combined peak flow of 54 L/h on 12 July. Daily maximum volumes reached 446 L in 2022 and 1033 L in 2023 (Figure 6).

	Peak flow rate (L/h)		Daily max volume (L)
	Box 1	Box 2	
2022	45.4	30.5	446
2023	39.8	21.2	1033

Table 3: Flow rates peaks

The exponential recession curves (Eq.1) fit well with the observed daily events, with an average R^2 value of 0.93. ~~Values~~Curves with R^2 values below 0.8 were omitted from the analysis, resulting in 93 events (Figure 9). The 'a' coefficient shows a clear decreasing trend in time from values of ~~9~~7-10 to 5-8.5 in both 2022 and 2023 seasons (Figure 9), while the 'b' coefficient increases from values of b≈1 at the beginning of the melting season to values of b≈1.15 at the end of the season (Equations 2 and 3).

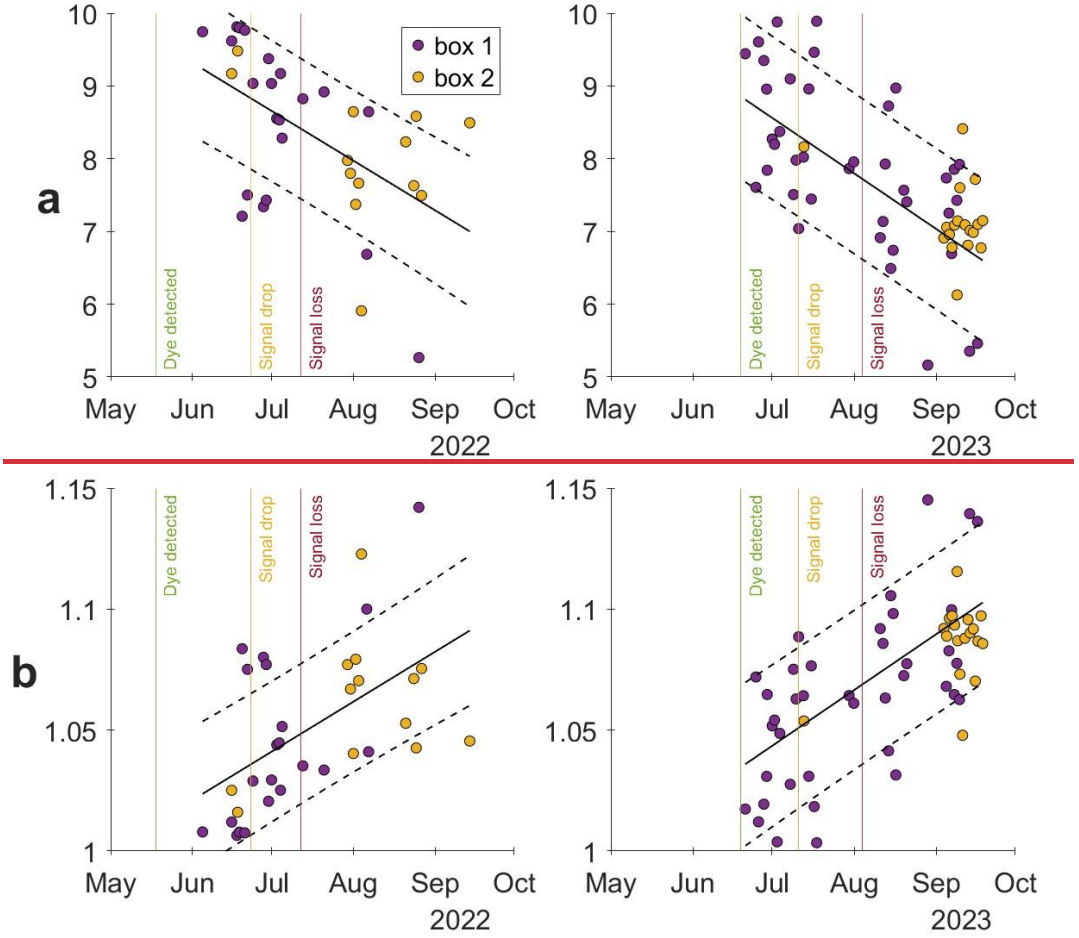
a
b
box 1
box 2
Dye detected
Signal drop
Signal loss
May
Jun
Jul
Aug
Sep
Oct
2022
2023

460

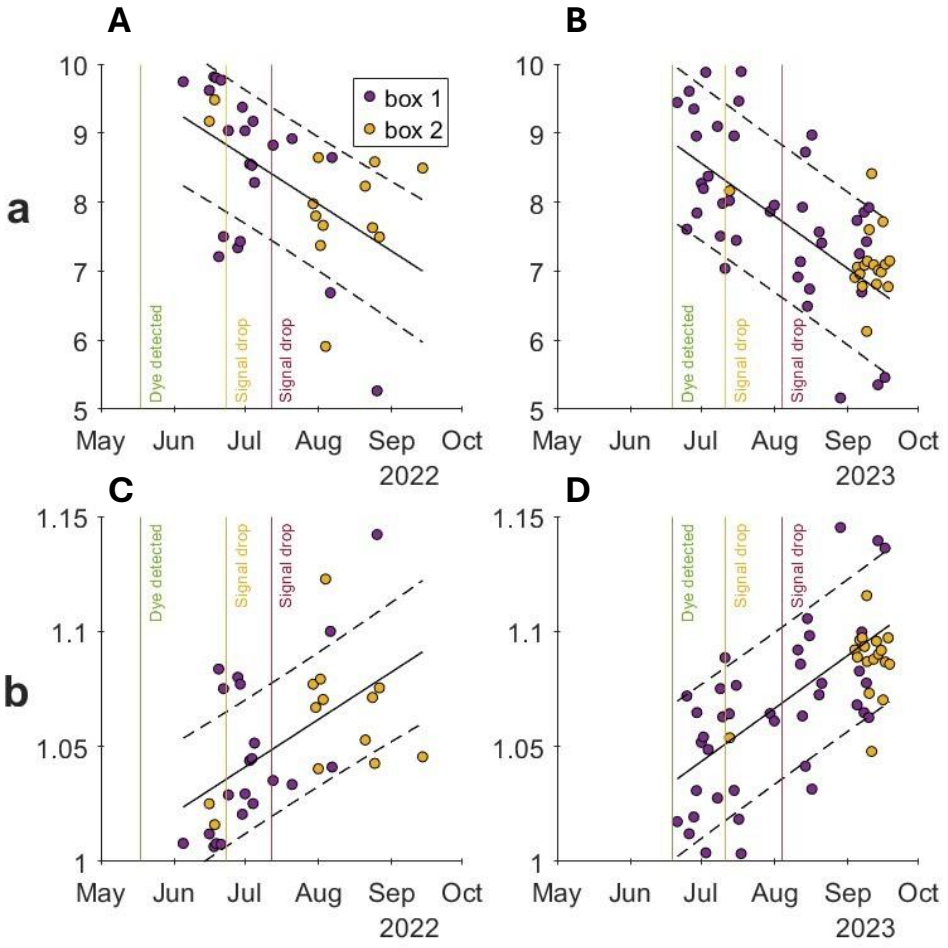

Figure 9~~: Values:~~ A-B) values of the 'a' coefficient of the recession ~~curve exponential coefficients a (top) and b (bottom)~~curves of flow events in 2022 (~~left~~and 2023 in box 1 (purple circles) and ~~2023 (right) vs. time.~~box 2 (yellow circles). C-D) values of the 'b' coefficient of the recession curves of flow events in 2022 and 2023 in box 1 (purple circles) and box 2 (yellow circles. Values obtained from curves with R^2 values below 0.~~75~~8 were omitted from the analysis. The black line is the linear regression of all the points (box 1 + box 2) with ±standard error (dashed black lines). The vertical lines indicate the timing of the detection of the fluorescent dye in the water that exits the fractures (green), the rapid drop of the signal intensity (orange), and the disappearance of the signal (red).

4.2. Snowpack evolution and water flow characteristics

Snowpack evolution is assessed through GST measurements at the snow-rock interface and using time-lapse pictures in 2023. Dampened daily oscillations in GST ~~are interpreted as~~indicate the presence of a snowpack with ~~sufficient insulating~~a significantinsulating effect. The melting period is generally visible as a zero-curtain period (*i.e* persisting 0 °C conditions at the rock-snow interface) (Hanson and Hoelzle, 2004) that lasts from several days to several weeks.

~~Measured~~Figure 5 displays the measured GST data at the rock-snow interface ~~are displayed in **Error! Reference source not found.**~~Figure 5. In 2022, the dampened daily oscillations are revealed by the similar values of mean and maximum GST, and the zero-curtain period is nearly nonexistent. This could be related to the early heat wave in 2022 that accelerated snow melting. Nonetheless, the first water flow events in May and early June 2022 occurred ~~with~~when GST ~~rising~~rose close to 0 °C, ~~hinting at~~demonstrating a link with snow melting. The first significant water flow event in 2022, which is also the greatest one~~,~~ with values reaching ~~>~~over 400 L/day, coincides with the transition to positive GST around mid-June. Summer precipitation episodes are suggested when water flow events follow periods with limited water ~~flows~~flow and ~~high~~positive GST and AT, such as in late July 2022. In 2023, the effect of snow cover on GST patterns is more evident, with an initial period of non-existent daily oscillations followed by a zero-curtain period until mid-July. ~~First~~The first flow events occurred during the onset of the snow melting period, with the highest peak of water flow reaching > 1000 L/day at the end of the zero-curtain period.

4.3. Fluorescence

4.3.1. Real-time fluorescence monitoring

In 2022, the real-time fluorescence sensor shows a strong signal of amino acid-G that followed the very first flow events in mid-May 2022 (Figure 7) and the sporadic flow events that followed it until 11 June 2022. The high amino acid-G signal continued with the onset of continuous water flows around mid-June 2022, until the rapid decrease at the end of June. The disappearance of the fluorescent signal, despite the sustained water flow likely corresponds to the complete melting of the lower terrace snowpack that contained the amino acid-G tracer, as seen in the photos from the time lapse camera (Figure 5). A weak signal of amino acid-G was detected until ~~the middle of~~ mid-July 2022 when both the fluorescence and flow rates diminished. ~~The~~This period of weak amino acid-G signal in the water could indicate dilution with water from precipitation that occurred after the dye was inserted or another not-dyed source (either late snow or rain).

No signal of the sulphorhodamine-B tracer inserted in the upper ledge was found. This could be due to excess dilution of the tracer solution with the snowmelt water to concentrations that were below the sensor sensitivity. A second hypothesis is that snowmelt from the upper terrace did not reach the fracture. ~~In 2023, a different dye was used (fluorescein), with a significantly higher concentration (see Sect. 3.1), and was clearly detected, suggesting that the absence of sulphorhodamine-B signal in 2022 was due to dilution.~~

In 2023, the amino acid-G signal was also detected in the first water flows on 19 June ~~2023~~. From the 24 June 2023 onwards, the signal of the fluorescein dye~~,~~ was detected alongside amino acid-G, which likely ~~confirming~~confirms that the concentration in sulphorhodamine-B was probably too low in 2022. The fluorescein signal is shorter than the amino acid-G signal, with a single high peak in the last week of June followed by a rapid decrease to low values. This could be explained by the different pathways from the upper terrace snowpack through the fracture network, together with the effect of low dispersivity of fluorescein. The high peaks of amino acid-G ~~high peaks~~ persisted continuously until ~~the 8th of~~8 July. Afterward, both tracers

remained in low concentrations until the end of July, suggesting that much of the ~~snow that had fallen during the~~ winter and spring ~~was removed~~snow had melted by ~~the 27th of~~27 July. That could mean that ~~all the~~the time needed for the entire winter snowpack ~~infiltration time~~ to infiltrate is ~~a little bit~~slightly more than ~~one~~a month. ~~Thereafter~~After that, the water ~~that flowed after the~~flowing from mid-~~end of~~ to late July was either direct precipitation (rain and snow) or possibly ~~melting of~~meltwater from ice that predated the tracer insertion ~~of the tracers~~.

4.3.2. ~~—~~ Fluorescence laboratory results

Additional analyses ~~were carried out in the laboratory on~~of water samples collected between May and mid-July 2023 from Boxes 1 and 2 and various fractures dripping into the ~~galleries~~tunnels of AdM~~.~~

~~Analyses done with~~ were carried out using a high sensitivity spectrophotometer in the EDYTEM laboratory. The results are similar and confirm ~~the results~~those found ~~from~~using the TRAQUA real-time sensor in Box 1. The signals for Fluorescein and amino-G show peaks at the same periods, i.e. at the end of the month of June and the beginning of July. The fluorescein signal is very short-lived, unlike amino-G, which continues to appear for a longer period. Samples from other locations in the ~~gallery did not~~tunnel show ~~a~~no signal of any of the fluorescent dyes.

4.4. Stable isotopes

Analysis of oxygen and hydrogen isotopes in the water samples shows that $\delta^{18}O$ and δD values range between -3.2‰ to -10‰ and -15‰ to -73‰ respectively (Figure 10). Excluding two samples, the $\delta^{18}O/\delta D$ ratio in all the water samples fall close to the global meteoric water line (GMWL) or align on a straight line parallel to the GMWL, likely because of a seasonal evolution of the local meteoric line from the GMWL (i.e. ~~). These values~~three samples taken on 22 September -labeled _22SEP). Two samples taken on 28 July 2022 from Box 2 deviate significantly below the GMWL (BOX2_28JUL – directly from the fracture, BCKT2_28JUL – from a 5L bucket that collected the water from the fracture) (Figure 10). This suggests that the water emerging from the fracture above Box 2 on that day was not of recent meteoric origin.

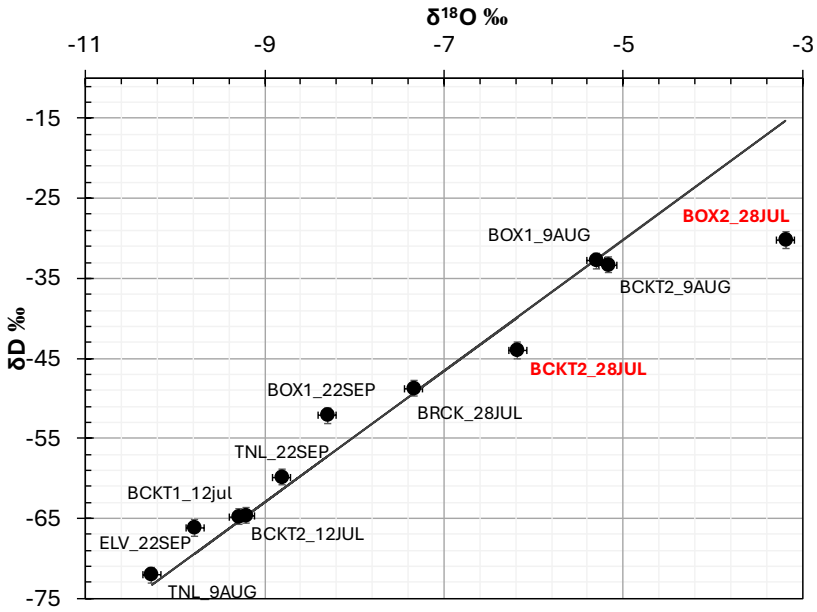

~~are consistent with those reported in high-elevation mountain regions, such as the Alps (Lauber and Goldscheider, 2014), the Pyrenees (Herms et al., 2019), and Northern China mountains (Sun et al., 2016). Excluding two samples, the $\delta^{18}O/\delta D$ ratio in all the water samples fall close to the global meteoric water line (GMWL) or align on a straight line parallel to the GMWL, likely because of a seasonal evolution of the local meteoric line from the GMWL (i.e. three samples taken on the 22nd of September -labeled _22SEP). Two samples taken on the 28th July 2022 from Box 2 deviate significantly below the GMWL (BOX2_28JUL – directly from the fracture, BCKT2_28JUL – from a 5L bucket that collected the water from the fracture) (Figure 9). This suggests that the water emerging from the fracture above Box 2 on that day was not of recent meteoric origin. A possible explanation is an extended residence time within the fracture system, allowing for interactions with the surrounding rock. Water samples collected during the peak of summer, on July 28 (BOX2_28JUL, BCKT2_28JUL) and August 9 (BOX1_9AUG, BCKT2_9AUG), from both collection systems (Box 1 and Box 2) exhibit relatively enriched $\delta^{18}O$ and δD values compared to those taken in early summer and fall. This enrichment may indicate the partial melting of seasonal snow. In contrast, two other samples from different locations within the AdM galleries (TNL_9AUG and BRCK_28JUL), collected on the same dates, do not show this enrichment. The observed $\delta^{18}O$ and δD enrichment during summer is consistent with findings from the Alps (Lauber and Goldscheider, 2014; Novel, 1995).~~

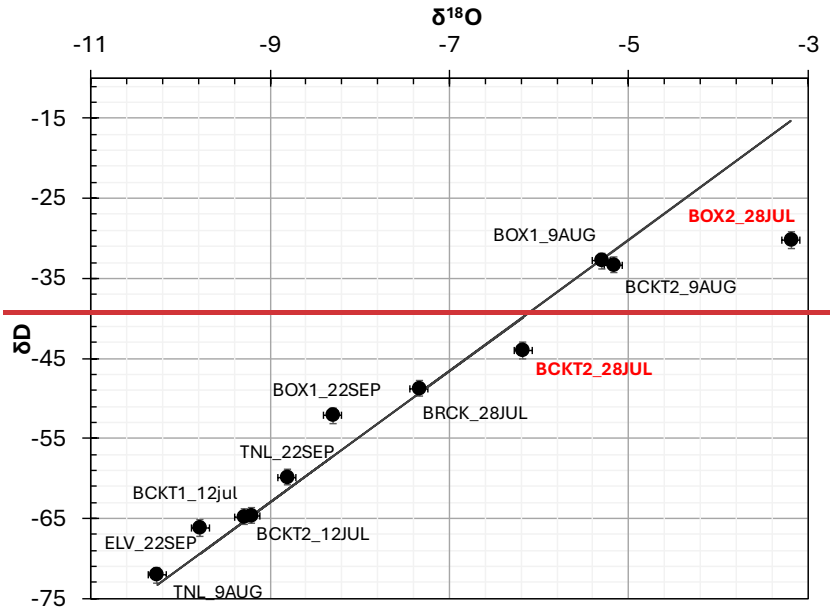

Figure 10: Stable isotopes $\delta^{18}O$ and δD in water samples. Note the two outliers (labeled in red) from the global meteoric water line (GMWL, black line) in samples taken from Box 2 on ~~the 28th of~~28 July 2022.

4.5. Water electrical conductivity

Electrical conductivity values are provided as maximum values per day of flow, ~~corrected at~~ after correction to a standard temperature of 25°C.

The ~~results of~~ electrical conductivity measurements from the 2022 season were unreliable due to the erroneous installation of the sensor. ~~Only results from~~Therefore, only the 2023 results are ~~thus~~ presented and analyzed (Figure 7). Overall, the conductivity values were far above the benchmark value measured in melted snow samples (9.2 µS/cm). On the continuous measurement (real-time monitoring system), the electrical conductivity of the water flowing into Box 1 ~~was~~remained relatively constant from mid-June to mid-July, with daily oscillations between 10-55 µS/cm and a general decreasing trend. The daily oscillations correlate with flow rate in a reverse relation – when flow rate is high the conductivity decreases (Figure 7). These values of conductivity correspond to the period of continuous cyclic flow rate in Box 1 that ended with the complete thaw of the winter snowpack~~).~~. Interestingly, significantly higher conductivities were measured at other locations in the ~~galleries, such as to~~ tunnels. Conductivity measurements with values of 485 µS/cm were taken in a tunnel wall under the west face of the central peak, from mid-July onwards, and 430 µS/cm (measured in 2022) at another location ~~along the "brick wall"~~in a tunnel under the north-east face of the central peak, near the ~~Hellbronner terrace.~~exit of the cable car going to Pointe Helbronner (Italy).

4.6. Water temperature

~~The temperature of the water during~~During flow events, the water temperature measured in two locations at outputs from the fractures ranges between 0 °C and 13 °C with an average of 6.1 °C (Figure 11). Measurements ~~made~~taken during periods without flow or subzero temperatures were removed from the analysis. Average GST and ~~ATs~~AT during the thawing season (15 May to 15 September) are close to 0 °C. ~~Measurements taken~~Values measured at the rock surface in the ~~gallery~~tunnel walls, near the fractures, during flow events show an intermediate mean value of 3.0 °C.

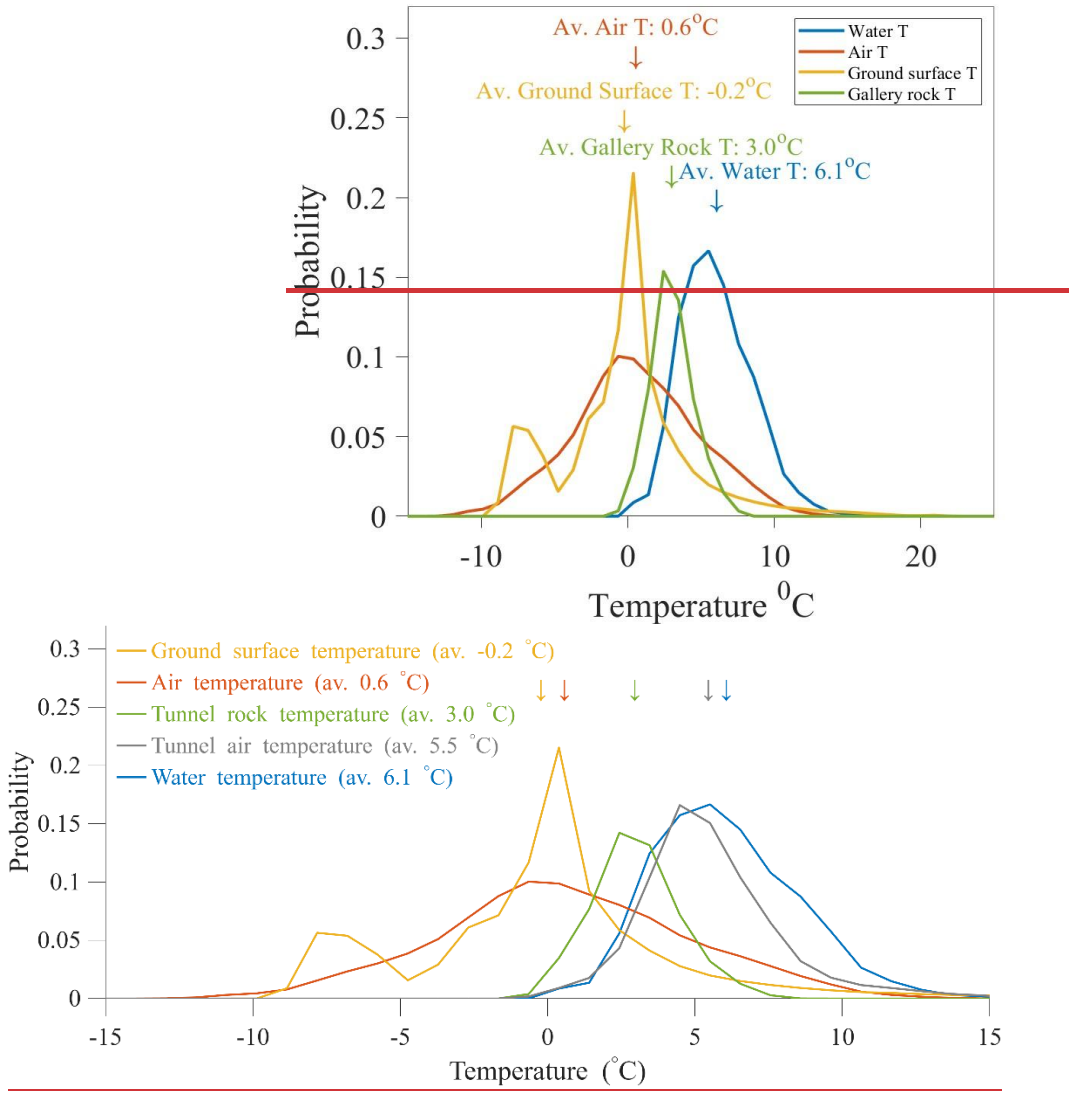

Figure 11~~: Distribution~~: Probability distribution of temperatures monitored during flow events (blue), atmospheric ATs (orange), ground surface temperatures (yellow), ~~and gallery~~tunnel wall (green~~).~~), and tunnel air. All distributions show data from the thawing season in 2022 and 2023 (15 May – 15 September). Note that the water ~~T~~temperature distribution (blue) shows only data when water

flow was detected in the monitoring system, while the other ~~T~~temperature distributions represent the entire data within the thawing season. The arrows show the location of the mean values on the horizontal axis.

5. Discussion

5.1. Water flows and weather conditions

Our results show rare evidence of highly effective surface-subsurface connectivity in steep permafrost-affected slopes, and strong ~~climatic~~weather signals in both seasonal and diurnal scales. ~~We see~~There is a clear link between the timing of ~~ATs~~AT and GST becoming positive in the early summer months and the onset of water flow. The first flow events in the season, which appeared in early May (2022) and June (2023), display a clear signal of the dye tracer and are directly linked to snow melting occurring under positive AT in the relatively shaded north-exposed rock face.

In both years, the onset of water flow in the fractures occurred when the daytime ~~ATs~~AT reached values above 0 °C. This change in temperature to positive values directly induced the melting of the snow that was deposited during winter, and its infiltration into the fractures. The melting of the snowpack is demonstrated by the simultaneous detection of the fluorescent dye tracers injected into the snowpack and the zero-curtain effect observed in the GST (Figure 5, Figure 7). The melting ~~of the snowpack~~ accelerated when the rock surface was exposed to heat flux from the atmosphere and ~~temperatures~~GST turned positive. From this point onwards, water flow behavior became more uniform, with regular daily oscillations, and reached the highest flow rates. Subsequently, after the exposure of the rock surface, some of the water in the fracture was directly from ~~direct~~ precipitation, which likely melted rapidly on the rock surface as the temperature increased, often above 0 °C. Each year, water flow in the fractures ceased when the temperature became negative again ~~during the fall months, and~~in autumn, with icicles ~~appeared~~appearing in the fractures.

Based on the 2-year monitoring, we conclude that water flow processes in high mountain rock faces are therefore seasonal, directly linked to the change ~~of air and surface temperatures above 0 °C during the summer period and below 0 °C during fall. The continuous detection of the dye, together with an analysis of time-lapse photos of the rock face and the shift of GST to positive values, show that snowmelt is the main source of water in the fractures during the early and main stages of flow, and contributes most of the water.~~in air and surface temperatures to above 0 °C during the summer period and below 0 °C during fall. The continuous detection of the dye, together with an analysis of time-lapse photos of the rock face and the shift of GST to positive values, show that snowmelt is the main source of water in the fractures during the early and main stages of flow, and contributes most of the water. This is consistent with similar observations reported by Scandroglio et al. (2025).

GST and AT also control flow rate oscillations on a daily time scale~~. The rapid increase observed in flow rate in the afternoon, followed by peak rate in the evening,~~ and ~~a long recession to significantly low flow in the early morning is~~ are cross-correlated with ~~the peak of air AT and GST with~~ a lag time of 3-9 and 0-~~3 hour~~6 hours, respectively (Table 2, Figure 8, Figure S3). ~~The~~

high sensitivity of water flowing in the fractures to surface temperatures is also demonstrated on July 6th 2023, when a single day with temperatures drop below 0 °C leads to a complete stop in water flow. The observedThese lag time enablestimes provide an estimation of the time taken for water to travel time through the fracture system, and allowsallow a rough approximation of flow velocity on the order of ~10 m10 m/hr.

The observed acceleration in flow rate coincides with the heating of the rock surface to >above 0 °C and the possiblepoints to a top-down thawing of the active layer (i.e. the near-surface layer that freezes and thaws through summer).

Nevertheless, the time lag between surface signal and water flow as well as the thawing of the active layer must be cautiously considered as it is possibly influenced by the open-system of the gallerytunnel causing an open flow path and a thermal shortcut allowing for bottom-up heat transfer. In addition, the touristic infrastructure and human presence can contribute to internal heat sources, including heating systems, the elevator motor, and body heat from visitors (Figure 11).

5.1.1. Heat waves effect

The contrast in summer conditions between 2022 and 2023 further illustrates that climaticthe strong influence of weather conditions strongly influenceon the timing and characteristics of the water flow period (Sect. 2.2). This is well demonstrated inby the effect of the early heat wave in spring 2022 that resulted in an early onset of water flows and the late heat wave in autumn 2023 that extended the water flow period much later in the season. The 2023 season was significantly wetter in terms of precipitation, and subsequently, more water flowed in the monitored fractures. However, when comparing the monthly distribution of flow during the thawing season, we find reveals that it was greatly influenced by the heat waves. Between May to mid-July, flow volume in 2022 was much higher than in the same period in 2023, as a result of the early and rapid thawing. Only in late August, did the total volume of water flow surpass that of 2022 (Figure 6). This raises an interesting point for future research on the influence of early vs. late water infiltration in permafrost rocks and the impact on hillslope processes. Assuming that water that infiltrates later in the season is warmer than the rock mass, and the infiltration paths contain less ice, it can potentially accelerate permafrost degradation and deepeningthickening of the active layer.

The rapid thawing in 2022, compared withCompared to the thawing in "normal" less extreme spring temperatures in 2023, the spring of 2023rapid thaw in 2022 is demonstratedevident in the GST data and in the lackabsence of a zero-curtain period that, which is seenclearly observed in the 2023 data (Figure 7). The zero-curtain likely represents a thawing period in which the snow absorbs latent heat from the atmosphere during the phase transition.Figure 5, Figure 7). We suggest that during the early heatwave in 2022, there was less snow, the thawing was very rapid, and the latent heat was absorbed rapidly. This can be seen in Figure 5, which shows less snow cover in min-June 2022 in comparison with mid-June 2023, and a large volume of water immediately after GST turns positive in mid-June 2022.

5.2. Water flow path conditions

~~Our results also demonstrate that an effective pathway is available in the fractures network for the infiltration of water from snowpack melting at the end of spring. The presence of fluorescent dye in the first water flow shows that the transfer rate is high. Furthermore, it seems that when the water flow stops at the end of fall, and icicles form in the fracture outlet, the flow is unsaturated. This unsaturated flow shows that there are preferential flow paths into the fractures, leading to open paths available for the melting water of the snowpack in the following spring. However, here again, we cannot overrule the possibility that the man-made space of the gallery contributed to the unsaturated conditions. In natural conditions, if undrained conditions occur, water could accumulate in the fractures, refreeze inside, and seal them. From a geomorphological perspective, artificial prevention of ice accumulation can inhibit fracture development through ice segregation and the related cryostatic pressure (Draebing et al., 2014; Draebing and Krautblatter, 2019; Hales and Roering, 2007; Hallet et al., 1991; Matsuoka and Murton, 2008; Matsuoka and Sakai, 1999). Completing these water flow observations with crack-meters measuring fractures rheology would provide an interesting perspective to clarify the role of the gallery, but this would require well identifying the fractures that are directly connected to the gallery.~~

Our results also indicate that an effective pathway exists within the fracture network through which the water released by snowpack melt can infiltrate at the end of spring. The early detection of fluorescent dye in the first flow events suggests a relatively rapid transfer from the surface to the fractures. Furthermore, when flow ceases at the end of autumn and icicles form at the fracture outlet, the observed flow appears to be unsaturated. In such cases, the unsaturated flow is likely routed through preferential pathways within the fracture system, which in turn suggests that at least part of the network remains open and able to convey meltwater during the following spring. However, we cannot overrule the possibility that the man-made space of the tunnel contributed to the unsaturated conditions. In natural conditions, if undrained conditions occur, water could accumulate in the fractures, refreeze inside them, and seal them off. Artificial prevention of ice accumulation can inhibit fracture development through ice segregation and the related cryostatic pressure (Draebing et al., 2014; Draebing and Krautblatter, 2019; Hales and Roering, 2007; Hallet et al., 1991; Matsuoka and Murton, 2008; Matsuoka and Sakai, 1999). Completing these water flow observations with crack-meters to measure fracture rheology would provide an interesting perspective to clarify the role of the tunnel. However, this would require to identify the fractures that are directly connected to the tunnel.

Interestingly, our monitoring system shows different but consistent timing of water flows in ~~Box~~Boxes 1 and ~~in Box~~ 2, ~~although they are~~despite them being located only a few meters ~~away~~apart (~~Figure 6~~Figure 6). One reason for the delayed flow in Box 2 could be linked to the location of the draining area closer to the colder north face, while the draining area of Box 1 is closer to the west face, which ~~is exposed to~~receives more solar radiation. Another explanation could be suggested based on the observed accumulation of sediments in Box 2, which was not observed in Box 1. The origin of the sand-size sediments observed in Box 2 is very likely from the erosion of the granite rock. ~~That would suggest~~This suggests that the fracture system ~~that is~~ drained to Box 2 is filled with sediments that reduce the hydraulic conductivity. However, ~~it seems that after the onset of~~once flow begins in Box 2, it responds directly ~~responds~~ to precipitation and positive AT and reaches high flow rates, ~~like~~similar to those

measured in Box 1 (e.g. in September 2023, ~~Figure 6).~~Figure 6, Figure 7). This supports the first ~~explanation~~hypothesis of different ~~exposure~~exposures to solar radiation. The effect of the sediments filling on the hydraulic conductivity is thus reduced in late summer, perhaps ~~by~~due to the thawing of ice-filled pores ~~in~~within the sediments filling. Alternatively, the sand and ice in the sub-vertical fractures might act as a partial plug ~~which~~that accumulates water above the infill. When the hydraulic head is high and the ice filling is thawing, the plug can break, allowing the sand ~~is~~to be transported, and causing a change in the flow regime ~~changes~~ (as it was observed in ~~box~~Box 2).

Based on the delayed onset of flow into Box 2 and the different flow behavior when compared with Box 1, we suggest that the two boxes collect two different flow pathways ~~with~~which have some common parts. ~~Because~~As Box 1 and Box 2 are located ~~close to one another (~~approximately 3 m ~~long distance),~~apart, we suggest that ~~under the north face,~~ the fracture network is complex~~;~~ under the north face. Some parts of the network contain sand-size sediments, ~~explaining~~which probably explain the late and lower flow of Box 2~~, while other~~. Other parts ~~are without any~~of the network lack sand filling and have a different hydraulic behavior. The effect of the sediment infill on ~~the~~ fracture hydrology should be investigated ~~in~~ further ~~work~~.

5.3. Deciphering possible water sources

According to the fluorescence data and the water flow timing, much of the collected water ~~is~~originates directly ~~originated~~ from recent snowmelt. This is also supported by the ~~analysis of~~ stable isotopes ~~in~~analysis of water samples from Box 1 (Figure 10) which display values that are consistent with those reported in high-elevation mountain regions, such as the Alps (Lauber and Goldscheider, 2014), the Pyrenees (Herms et al., 2019), and Northern China mountains (Sun et al., 2016). ~~). It is also very likely that direct rain in late summer infiltrates the rock fractures.~~It is also very likely that rain in late summer infiltrated the rock fractures and contributed to the flow. However, some data also hints at other possible sources of water. First, even the lowest values of electric conductivity of the water are far above the expected snow melt conductivity and they steadily rise with decreasing flow rate~~, as often observed in aquifers.~~. The surprisingly high electric conductivity found in some samples collected from fractures (>400 µS/cm) can point to long residence times in the rock. Considering the results from the fluorescent dyes and the hydrological behavior, the flow path is very short (in both distance and ~~in~~ time), thus ruling out a long exchange time between the surface water and the rock. ~~An alternative explanation~~It is possible that recent meteoric water ~~is~~was mixed with older water that was trapped as ice in the permafrost-affected rocks. This is also supported by the observed change in the ~~form~~shape of the recession curves ~~with~~over time (Figure 9). The recession curves at the beginning of the melting season (May-June) show values of b≈1 and fit well with the exponential form that is expressed in Equation 1. The early-season recession curves are also characterized by high values of 'a'. Over time, the value of 'b' increases linearly to a form better described by Equation 3, while the value of the 'a' coefficient decreases. This change in recession form~~,~~ (Figure S4), from aquifer-type (Equation 1) to channel-type (Equation 3) can be explained by the thawing of ice in wide sub-vertical fractures that are likely to react more individually (rather than as a network) and enable rapid flow in the fractured granite. The decrease of 'a' is non-trivial since one could expect that the drainage would be more efficient and with shorter recession time (i.e. higher

‘a’ values) as the thawing of ice in the rock fractures progresses. We thus suggest that the observed decrease in ‘a’ is due to a gradual change in the water source. As less water drains from the surface (after the complete thawing of the winter snow) and more water drains from the subsurface ice trapped in the fractures, the hydraulic gradient is reduced, and the duration of the recession is extended. Another evidence of a possible fossilized source ~~is~~can be seen in samples collected from Box 2 on ~~the 28th of~~28 July (BOX2_28JUL, BCKT2_28JUL) which ~~shows~~show an isotopic signal that is distant from the meteoric water line (Figure 10). One possible explanation is an extended residence time within the fracture system, allowing for interactions with the surrounding rock. Water samples collected during the peak of summer, on July 28 (BOX2_28JUL, BCKT2_28JUL) and August 9 (BOX1_9AUG, BCKT2_9AUG), from both collection systems (Box 1 and Box 2) exhibit relatively enriched $\delta^{18}O$ and δD values compared to those taken in early summer and fall. This enrichment may indicate the partial melting of seasonal snow.). In contrast, two other samples from different locations within the AdM tunnels (TNL_9AUG and BRCK_28JUL), collected on the same dates, do not show this enrichment. The observed $\delta^{18}O$ and δD enrichment during summer is consistent with findings from the Alps (Lauber and Goldscheider, 2014; Novel, 1995).

From a permafrost perspective, the thawing of large volumes of fossilized water in permafrost-affected rock ~~in large volumes~~ could be related to a ~~deepening~~thickening of the active layer and degradation of high mountain permafrost - a regional phenomenon seen in recent decades in boreholes in the Alps and other mountain ranges (Magnin et al., 2024; Noetzli et al., 2024), but never observed directly in water samples from fractures.

The absence of a signal from sulphorhodamine-B tracer in the water from the upper ledge could be due to excess dilution of the tracer solution with the snowmelt water, resulting in concentrations below the sensor sensitivity. In 2023, a different dye was used (fluorescein), with a significantly higher concentration (see Sect. 3.1), and was clearly detected, confirming that the absence of a sulphorhodamine-B signal in 2022 was due to dilution.

5.4. Implications for alpine geomorphology, hydrogeology, and permafrost

The quantity, timing, and characteristics of water that infiltrates in the fractured, permafrost-affected rocks are important factors in many geomorphological, hydrological, and geomechanical processes~~, but~~. However, our understanding of the parameters controlling these factors is ~~poor, and~~ limited, as is the ability to measure them ~~is very limited~~. For example, the timing and quantity of water availability from snowmelt are often estimated indirectly using numerical models of energy and water mass balance ~~(Ben-Asher et al., 2023; Leinauer et al., 2021)~~(Ben-Asher et al., 2023; Lehning et al., 1999; Leinauer et al., 2021) and snowpack physics (Lehning et al., 1999; Vionnet et al., 2012). However, the ~~results~~outputs of ~~these simulations are highly sensitive to~~ such models depend strongly on the meteorological ~~forcings~~forcing used to drive them, and on hydrogeological parameters that are usually ~~highly uncertain.~~poorly constrained. The results of this study provide direct observations that can ~~profoundly~~ help to reduce these uncertainties and improve ~~the~~our understanding of water availability for infiltration and ~~the influence of~~its environmental ~~parameters~~controls.

~~The new information we provide on water flow in permafrost rock fractures can also be used to improve coupled heat and water flow models by providing the parameters needed to calculate heat advection from the surface (flow rate and water temperature). The average water temperature measured during flow events is 6.1 °C. Theoretical hydrodynamic thermal models suggested that the flow of water with temperatures above 5 °C is efficient in thawing permafrost-affected rocks along fractures (Magnin and Josnin, 2021).~~

The new information that we provide regarding water flow in permafrost rock fractures can also be used to improve coupled heat and water flow models, as it provides the parameters needed to calculate heat advection from the surface (flow rate and water temperature). The average water temperature measured during flow events is 6.1 °C (Figure 11).

Several recent studies ~~suggested~~suggest that water-related processes are driving rockwall instability in mountain permafrost (Cathala et al., 2024; Gruber et al., 2004; Krautblatter et al., 2012; Magnin and Josnin, 2021). Analysis of 1152 rockfall events in the Mont Blanc massif between 2015-2021 (Magnin et al., 2023; Ravanel and Deline, 2013) ~~show~~shows that 96% of the events occurred between June and September, with the highest numbers in July, before the maximum depth of the seasonal active layer was reached (Magnin et al., 2023), possibly due to enhanced water flows when snow melts in the early summer.

The cable car to ~~Aiguille du Midi~~AdM has been operating since ~~1950's~~the 1950s. The staff of the operating company of the site reported that significant water flow from the fractures in the ~~gallery started~~tunnel began in the particularly hot summer of 2015. ~~The~~While the reason for the initiation of the observed seasonal flow ~~is unknown, but~~remains unclear, it is reasonable to suggest that it is related to the gradual heating of the rock mass in AdM and the development of the active layer that is observed in monitored boreholes in the site (Magnin et al., 2024). ~~It points to the possibility~~This suggests that the environmental conditions in AdM are in a transient state~~,~~ and have reached a threshold that triggers substantial water availability to fractures in the permafrost rocks.

5.5. Outlook and Future Directions

Future investigations could build upon this study by conducting more detailed chemical analyses of dissolved elements, which would help constrain water–rock interaction processes and potential solute sources. Characterizing the mineralogy and size distribution of sediments flushed from fractures could provide complementary evidence regarding transport pathways and mechanical erosion. Further stable isotope analyses, combined with absolute dating techniques (e.g., tritium–helium, radiocarbon, or noble gas methods), could enable a clearer distinction to be made between modern meltwater, rainfall, and contributions from older subsurface ice. Together, these approaches would refine our understanding of fracture-scale hydrology in steep permafrost rock walls and how sensitive it is to climate change.

6. Conclusions

This study presents novel, direct observations of water infiltration in a high mountain permafrost rock wall, providing rare field data on processes that are typically poorly understood and rarely monitored. ~~Using a~~A two-year monitoring system was installed inside man-made tunnels at the Aiguille du Midi (~~3842 m~~3842 m a.s.l.) in the Mont Blanc massif~~, we tracked~~ to track real-time water flow, temperature, electrical conductivity, and the infiltration of fluorescent tracers injected into the overlying snowpack. These measurements were then combined with GST and meteorological data to investigate the origin, timing, and dynamics of water flow in permafrost-affected fractured rock.

Our main findings are:

- Water flow in fractures is seasonal and ~~began~~begins when AT exceeded 0 °C. Steady flow with daily oscillations ~~started~~began when GST rose above 0°C, which occurred several weeks (in 2022~~),~~) or ~~several~~ days (in 2023) after the initiation of flow ~~and~~.
- This flow contained the dye tracer that had been inserted ~~in~~into the snowpack above the ~~gallery~~tunnel.
- Fluorescent tracers were detected in the first water flow in early summer and in the flow that followed until mid-summer. This confirms that the main source of water is snowmelt from the winter snowpack ~~is the main source of water~~.
- In snow-free conditions, during late summer, rain also contributes to the flow.
- The peak flow shows short lag times relative to the peaks of air and ground temperatures (3–9 h and 0–3 h, respectively), indicating rapid, unsaturated infiltration pathways.
- Evidence from electrical conductivity measurements, stable water isotopes, and analysis of recession curves suggests that water stored in the rock is contributing to the flow, possibly from the ~~thawing~~melting of older ice ~~in~~within the fracture system. ~~The question of~~Further investigation is needed to determine the origin of water with high electrical conductivity and a unique isotopic signature ~~needs further investigation.~~. However, if confirmed, it would provide direct evidence of the melting of fossil ~~water released with~~ice and permafrost degradation.
- Distinct flow regimes of flow collected from two nearby fractures in ~~Box~~Boxes 1 ~~and Box~~ 2 demonstrate a heterogeneous fracture network with varying sediment infill. It reveals the existence of fractures directly linked to the surface on the one hand, and fractures with sand infill and likely ice fill with a longer transfer time on the other hand. Moreover, the hydraulic characteristics of the fractures show unsaturated flow with preferential paths at the end of each warm season before the active layer freezes again.
- Water temperatures often exceed ~~5~~ 5 °C; ~~altogether~~together with the intense water flow measured, it strongly ~~suggest~~suggests that ~~-~~ advective heat transfer likely contributes to ice melting within the rock mass.

This work ~~offers~~provides direct empirical evidence of how surface water infiltrates permafrost rock walls and interacts with the surface and internal fracture systems. These findings are ~~critical~~crucial for the development of coupled hydro-thermal models and understanding how climate warming affects permafrost degradation, water pathways, and slope stability. ~~The~~This approach and its results can help future studies ~~aiming~~that aim to characterize hydrogeological processes in high-

~~altitude~~elevation rock fractures, identify early signs of geomorphic instability, and assess the vulnerability of alpine permafrost landscapes ~~under continued~~in the context of ongoing climate change.

Author contribution

MB, JYJ, FM: Conceptualization, Data curation, Investigation, Formal analysis, Methodology, Writing.
AC: Data curation, Investigation, Formal analysis, Methodology, Writing.
JB: Investigation, Writing.
EM: Investigation, Methodology.
AP: Resources.
YP: Data curation, Methodology.

Competing interests

The authors declare that they have no conflict of interest

Acknowledgements

We thank the Compagnie du Mont Blanc and the Aiguille du Midi station staff for their support and access to the site. We also thank UMR 1114 EMMAH laboratory (Environnement Méditerranéen et Modélisation des Agro-Hydrosystèmes) for the stable isotope analysis. We are grateful for the assistance of Marine Quiers in planning and applying fluorescence techniques. This research has been supported by the Agence Nationale de la Recherche (WISPER project, no. ANR-19-CE01-0018).

References

Allen, S. K., Gruber, S., and Owens, I. F.: Exploring steep bedrock permafrost and its relationship with recent slope failures in the Southern Alps of New Zealand, Permafr. Periglac. Process., 20, 345–356, https://doi.org/10.1002/ppp.658, 2009.

Bast, A., Kenner, R., and Phillips, M.: Short-term cooling, drying, and deceleration of an ice-rich rock glacier, The Cryosphere, 18, 3141–3158, https://doi.org/10.5194/tc-18-3141-2024, 2024.

Ben-Asher, M., Magnin, F., Westermann, S., Malet, E., Berthet, J., Bock, J., Ravanel, L., and Deline, P.: Estimating surface water availability in high mountain rock slopes using a numerical energy balance model, https://doi.org/10.5194/esurf-11-899-2023, 2023.

~~Bertini, G., Marcucci, M., Nevini, R., Passerini, P., and Sguazzoni, G.: Patterns of faulting in the Mont Blanc granite, Tectonophysics, 111, 65–106, https://doi.org/10.1016/0040-1951(85)90066-6, 1985.~~

Boussinesq, J.: Essai sur la théorie des eaux courantes, Impr. nationale, 1877.

Brennan, K. P., David, R. O., and Borduas-Dedekind, N.: Spatial and temporal variability in the ice-nucleating ability of alpine snowmelt and extension to frozen cloud fraction, Atmospheric Chem. Phys., 20, 163–180, https://doi.org/10.5194/acp-20-163-2020, 2020.

Brutsaert, W. and Nieber, J. L.: Regionalized drought flow hydrographs from a mature glaciated plateau, Water Resour. Res., 13, 637–643, https://doi.org/10.1029/WR013i003p00637, 1977.

Cathala, M., Bock, J., Magnin, F., Ravanel, L., Ben Asher, M., Astrade, L., Bodin, X., Chambon, G., Deline, P., Faug, T., Genuite, K., Jaillet, S., Josnin, J.-Y., Revil, A., and Richard, J.: Predisposing, triggering and runout processes at a permafrost-affected rock avalanche site in the French Alps (Étache, June 2020), Earth Surf. Process. Landf., 49, 3221–3247, https://doi.org/10.1002/esp.5881, 2024.

Copernicus Climate Change Service (C3S): European State of the Climate 2022, Copernicus Climate Change Service (C3S), https://doi.org/10.24381/GVAF-H066, 2023.

Copernicus Climate Change Service (C3S): European State of the Climate 2023, Copernicus Climate Change Service (C3S), https://doi.org/10.24381/BS9V-8C66, 2024.

Deline, P., Gruber, S., Delaloye, R., Fischer, L., Geertsema, M., Giardino, M., Hasler, A., Kirkbride, M., Krautblatter, M., Magnin, F., McColl, S., Ravanel, L., and Schoeneich, P.: Ice Loss and Slope Stability in High-Mountain Regions, in: Snow and Ice-Related Hazards, Risks, and Disasters, Elsevier, 521–561, https://doi.org/10.1016/B978-0-12-394849-6.00015-9, 2015.

Draebing, D. and Krautblatter, M.: The Efficacy of Frost Weathering Processes in Alpine Rockwalls, Geophys. Res. Lett., 46, 6516–6524, https://doi.org/10.1029/2019GL081981, 2019.

Draebing, D., Krautblatter, M., and Dikau, R.: Interaction of thermal and mechanical processes in steep permafrost rock walls: A conceptual approach, Geomorphology, 226, 226–235, https://doi.org/10.1016/j.geomorph.2014.08.009, 2014.

Dwivedi, R. D., Singh, P. K., Singh, T. N., and Singh, D. P.: Compressive strength and tensile strength of rocks at sub-zero temperature, Indian J. Eng. Mater. Sci., 5, 43–48, 1998.

Eppes, M. C. and Keanini, R.: Mechanical weathering and rock erosion by climate-dependent subcritical cracking, Rev. Geophys., 55, 470–508, https://doi.org/10.1002/2017RG000557, 2017.

Erismann, T. H. and Abele, G.: Dynamics of rockslides and rockfalls, Springer Science & Business Media, 2001.

Fey, C., Wichmann, V., and Zangerl, C.: Influence of permafrost degradation and glacier retreat on recent high mountain rockfall distribution in the eastern European Alps, Earth Surf. Process. Landf., 50, e70063, https://doi.org/10.1002/esp.70063, 2025.

Fischer, L., Amann, F., Moore, J. R., and Huggel, C.: Assessment of periglacial slope stability for the 1988 Tschierva rock avalanche (Piz Morteratsch, Switzerland), Eng. Geol., 116, 32–43, https://doi.org/10.1016/j.enggeo.2010.07.005, 2010.

Ford, D. and Williams, P.: Karst geomorphology and hydrology, 1st ed., Unwin Hyman, London, 42 pp., 1989.

Gabrielli, C. P., McDonnell, J. J., and Jarvis, W. T.: The role of bedrock groundwater in rainfall–runoff response at hillslope and catchment scales, J. Hydrol., 450–451, 117–133, https://doi.org/10.1016/j.jhydrol.2012.05.023, 2012.

Gardent, M., Rabatel, A., Dedieu, J.-P., and Deline, P.: Multitemporal glacier inventory of the French Alps from the late 1960s to the late 2000s, Glob. Planet. Change, 120, 24–37, https://doi.org/10.1016/j.gloplacha.2014.05.004, 2014.

Gruber, S. and Haeberli, W.: Permafrost in steep bedrock slopes and its temperatures-related destabilization following climate change, J. Geophys. Res. Earth Surf., 112, 1–10, https://doi.org/10.1029/2006JF000547, 2007.

Gruber, S., Hoelzle, M., and Haeberli, W.: Rock-wall temperatures in the Alps: Modelling their topographic distribution and regional differences, Permafr. Periglac. Process., 15, 299–307, https://doi.org/10.1002/ppp.501, 2004.

Guillet, G., Ravanel, L., Beutel, J., and Deline, P.: Fracture kinematics in steep bedrock permafrost, Aiguille du Midi (3842 m a.s.l., Chamonix Mont-Blanc, France), https://doi.org/10.3929/ETHZ-B-000309262, 2018.

Hales, T. C. and Roering, J. J.: Climatic controls on frost cracking and implications for the evolution of bedrock landscapes, J. Geophys. Res., 112, F02033–F02033, https://doi.org/10.1029/2006JF000616, 2007.

Hallet, B., Walder, J. S., and Stubbs, C. W.: Weathering by segregation ice growth in microcracks at sustained subzero temperatures: Verification from an experimental study using acoustic emissions, Permafr. Periglac. Process., 2, 283–300, https://doi.org/10.1002/ppp.3430020404, 1991.

Hanson, S. and Hoelzle, M.: The thermal regime of the active layer at the Murtèl rock glacier based on data from 2002, Permafr. Periglac. Process., 15, 273–282, https://doi.org/10.1002/ppp.499, 2004.

Hasler, A., Gruber, S., Font, M., and Dubois, A.: Advective heat transport in frozen rock clefts: Conceptual model, laboratory experiments and numerical simulation, Permafr. Periglac. Process., 22, 378–389, https://doi.org/10.1002/ppp.737, 2011.

Hasler, A., Gruber, S., and Beutel, J.: Kinematics of steep bedrock permafrost, J. Geophys. Res. Earth Surf., 117, 2011JF001981, https://doi.org/10.1029/2011JF001981, 2012.

Herms, I., Jódar, J., Soler, A., Vadillo, I., Lambán, L. J., Martos-Rosillo, S., Núñez, J. A., Arnó, G., and Jorge, J.: Contribution of isotopic research techniques to characterize high-mountain-Mediterranean karst aquifers: The Port del Comte (Eastern Pyrenees) aquifer, Sci. Total Environ., 656, 209–230, https://doi.org/10.1016/j.scitotenv.2018.11.188, 2019.

Huggel, C., Allen, S., Deline, P., Fischer, L., Noetzli, J., and Ravanel, L.: Ice thawing, mountains falling-are alpine rock slope failures increasing, Geol. Today, 28, 98–104, https://doi.org/10.1111/j.1365-2451.2012.00836.x, 2012.

Krakauer, N. Y. and Temimi, M.: Stream recession curves and storage variability in small watersheds, Hydrol. Earth Syst. Sci., 15, 2377–2389, https://doi.org/10.5194/hess-15-2377-2011, 2011.

Krautblatter, M., Huggel, C., Deline, P., and Hasler, A.: Research Perspectives on Unstable High-alpine Bedrock Permafrost: Measurement, Modelling and Process Understanding, Permafr. Periglac. Process., 23, 80–88, https://doi.org/10.1002/ppp.740, 2012.

Krautblatter, M., Funk, D., and Günzel, F. K.: Why permafrost rocks become unstable: A rock-ice-mechanical model in time and space, Earth Surf. Process. Landf., 38, 876–887, https://doi.org/10.1002/esp.3374, ~~2013a~~2013.

~~Krautblatter, M., Funk, D., and Günzel, F. K.: Why permafrost rocks become unstable: A rock-ice-mechanical model in time and space, Earth Surf. Process. Landf., 38, 876–887, https://doi.org/10.1002/esp.3374, 2013b.~~

Lauber, U. and Goldscheider, N.: Use of artificial and natural tracers to assess groundwater transit-time distribution and flow systems in a high-alpine karst system (Wetterstein Mountains, Germany), Hydrogeol. J., 22, 1807–1824, https://doi.org/10.1007/s10040-014-1173-6, 2014.

Legay, A., Magnin, F., and Ravanel, L.: Rock temperature prior to failure: Analysis of 209 rockfall events in the Mont Blanc massif (Western European Alps), Permafr. Periglac. Process., 32, 520–536, https://doi.org/10.1002/ppp.2110, 2021.

Lehning, M., Bartelt, P., Brown, B., Russi, T., Stöckli, U., and Zimmerli, M.: snowpack model calculations for avalanche warning based upon a new network of weather and snow stations, Cold Reg. Sci. Technol., 30, 145–157, https://doi.org/10.1016/S0165-232X(99)00022-1, 1999.

Leinauer, J., Jacobs, B., and Krautblatter, M.: High alpine geotechnical real time monitoring and early warning at a large imminent rock slope failure (Hochvogel, GER/AUT), IOP Conf. Ser. Earth Environ. Sci., 833, https://doi.org/10.1088/1755-1315/833/1/012146, 2021.

~~Leloup, P. H., Arnaud, N., Sobel, E. R., and Lacassin, R.: Alpine thermal and structural evolution of the highest external crystalline massif: The Mont Blanc: EXHUMATION OF THE MONT BLANC MASSIF, Tectonics, 24, n/a n/a, https://doi.org/10.1029/2004TC001676, 2005.~~

Li, N., Zhang, P., Chen, Y., and Swoboda, G.: Fatigue properties of cracked, saturated and frozen sandstone samples under cyclic loading, Int. J. Rock Mech. Min. Sci., 40, 145–150, https://doi.org/10.1016/S1365-1609(02)00111-9, 2003.

Magnin, F. and Josnin, J.-Y.: Water Flows in Rockwall Permafrost : a Numerical Approach Coupling Hydrological and Thermal Processes, J. Geophys. Res. Earth Surf., 2021.

Magnin, F., Brenning, A., Bodin, X., Deline, P., and Ravanel, L.: Modélisation statistique de la distribution du permafrost de paroi : application au massif du Mont Blanc, Géomorphologie Relief Process. Environ., 21, 145–162, https://doi.org/10.4000/geomorphologie.10965, 2015a.

Magnin, F., Deline, P., Ravanel, L., Noetzli, J., and Pogliotti, P.: Thermal characteristics of permafrost in the steep alpine rock walls of the Aiguille du Midi (Mont Blanc Massif, 3842 m a.s.l), Cryosphere, 9, 109–121, https://doi.org/10.5194/tc-9-109-2015, 2015b.

Magnin, F., Ravanel, L., Ben-Asher, M., Bock, J., Cathala, M., Duvillard, P.-A., Jean, P., Josnin, J.-Y., Kaushik, S., Revil, A., and Deline, P.: From Rockfall Observation to Operational Solutions: Nearly 20 years of Cryo-gravitational Hazard Studies in Mont-Blanc Massif, Rev. Géographie Alp., 111–2, https://doi.org/10.4000/rga.11703, 2023.

Magnin, F., Ravanel, L., Bodin, X., Deline, P., Malet, E., Krysiecki, J., and Schoeneich, P.: Main results of permafrost monitoring in the French Alps through the *PermaFrance* network over the period 2010–2022, Permafr. Periglac. Process., 35, 3–23, https://doi.org/10.1002/ppp.2209, 2024.

Maillet, E. T.: Essais d'hydraulique souterraine & fluviale, A. Hermann, 1905.

Manning, A. H. and Caine, J. S.: Groundwater noble gas, age, and temperature signatures in an Alpine watershed: Valuable tools in conceptual model development, Water Resour. Res., 43, 2006WR005349, https://doi.org/10.1029/2006WR005349, 2007.

Marcer, M., Ringsø Nielsen, S., Ribeyre, C., Kummert, M., Duvillard, P., Schoeneich, P., Bodin, X., and Genuite, K.: Investigating the slope failures at the Lou rock glacier front, French Alps, Permafr. Periglac. Process., 31, 15–30, https://doi.org/10.1002/ppp.2035, 2020.

Maréchal, J. C., Perrochet, P., and Tacher, L.: Long-term simulations of thermal and hydraulic characteristics in a mountain massif: The Mont Blanc case study, French and Italian Alps, Hydrogeol. J., 7, 341–354, https://doi.org/10.1007/s100400050207, 1999.

Maréchal, J.-C.: Les circulations d'eau dans les massifs cristallins alpins et leurs relations avec les ouvrages souterrains, EPFL, https://doi.org/10.5075/epfl-thesis-1769, 1998.

Matsuoka, N. and Murton, J.: Frost weathering: recent advances and future directions, Permafr. Periglac. Process., 19, 195–210, https://doi.org/10.1002/ppp.620, 2008.

Matsuoka, N. and Sakai, H.: Rockfall activity from an alpine cliff during thawing periods, Geomorphology, 28, 309–328, https://doi.org/10.1016/S0169-555X(98)00116-0, 1999.

Mellor, M.: Mechanical properties of rocks at low temperatures, in: 2nd International Conference on Permafrost, Yakutsk, International Permafrost Association, 334–344, 1973.

Noetzli, J., Isaksen, K., Barnett, J., Christiansen, H. H., Delaloye, R., Etzelmüller, B., Farinotti, D., Gallemann, T., Guglielmin, M., Hauck, C., Hilbich, C., Hoelzle, M., Lambiel, C., Magnin, F., Oliva, M., Paro, L., Pogliotti, P., Riedl, C., Schoeneich, P., Valt, M., Vieli, A., and Phillips, M.: Enhanced warming of European mountain permafrost in the early 21st century, Nat. Commun., 15, 10508, https://doi.org/10.1038/s41467-024-54831-9, 2024.

~~Novel, J. P.: Contribution de la géochimie à l'étude d'un aquifère alluvial de montagne: cas de la vallée d'Aoste Italie, PhD Thesis, Paris 6, 1995.~~

~~Raumer, J. F. von and Bussy, F.: Mont Blanc and Aiguilles Rouges geology of their polymetamorphic basement (external massifs, Westerns Alps, France Switzerland), Mém. Géologie Lausanne, 42, 1–210, 2004.~~

Pellet, C. and Hauck, C.: Monitoring soil moisture from middle to high elevation in Switzerland: set-up and first results from the SOMOMOUNT network, Hydrol. Earth Syst. Sci., 21, 3199–3220, https://doi.org/10.5194/hess-21-3199-2017, 2017.

Phillips, M., Haberkorn, A., Draebing, D., Krautblatter, M., Rhyner, H., and Kenner, R.: Seasonally intermittent water flow through deep fractures in an Alpine Rock Ridge: Gemsstock, Central Swiss Alps, Cold Reg. Sci. Technol., 125, 117–127, https://doi.org/10.1016/j.coldregions.2016.02.010, 2016.

Ravanel, L. and Deline, P.: Climate influence on rockfalls in high-alpine steep rockwalls: The north side of the aiguilles de chamonix (mont blanc massif) since the end of the "Little Ice Age," Holocene, 21, 357–365, https://doi.org/10.1177/0959683610374887, 2011.

Ravanel, L. and Deline, P.: A network of observers in the Mont-Blanc massif to study rockfall from high Alpine rockwalls, Geogr. Fis. E Din. Quat., 151–158, https://doi.org/10.4461/GFDQ.2013.36.12, 2013.

Ravanel, L., Magnin, F., and Deline, P.: Impacts of the 2003 and 2015 summer heatwaves on permafrost-affected rock-walls in the Mont Blanc massif, Sci. Total Environ., 609, 132–143, https://doi.org/10.1016/j.scitotenv.2017.07.055, 2017.

~~Rossi, M., Rolland, Y., Vidal, O., and Cox, S. F.: Geochemical variations and element transfer during shear zone development and related episyenites at middle crust depths: insights from the Mont Blanc granite (French – Italian Alps), Geol. Soc. Lond. Spec. Publ., 245, 373–396, https://doi.org/10.1144/GSL.SP.2005.245.01.18, 2005.~~

954 Scandroglio, R., Stoll, V., and Krautblatter, M.: The driving force of all nature. Modelling water pressure and its stability
955 consequences on alpine bedrock slopes, IOP Conf. Ser. Earth Environ. Sci., 833, https://doi.org/10.1088/1755-
956 1315/833/1/012109, 2021.

957 Scandroglio, R., Weber, S., Rehm, T., and Krautblatter, M.: Decadal in situ hydrological observations and empirical modeling
958 of pressure head in a high-alpine, fractured calcareous rock slope, Earth Surf. Dyn., 13, 295–314, https://doi.org/10.5194/esurf-
959 13-295-2025, 2025.

960 Scherler, M., Hauck, C., Hoelzle, M., Stähli, M., and Völksch, I.: Meltwater infiltration into the frozen active layer at an alpine
961 permafrost site, Permafr. Periglac. Process., 21, 325–334, https://doi.org/10.1002/ppp.694, 2010.

962 Smith, R. E. (Ed.): Infiltration theory for hydrologic applications, American Geophysical Union, Washington, DC, 1 pp.,
963 https://doi.org/10.1029/WM015, 2002.

964 Staub, B. and Delaloye, R.: Using Near-Surface Ground Temperature Data to Derive Snow Insulation and Melt Indices for
965 Mountain Permafrost Applications: Snow and Melt Indices Derived from GST Data, Permafr. Periglac. Process., 28, 237–248,
966 https://doi.org/10.1002/ppp.1890, 2017.

967 Strauhal, T., Loew, S., Holzmann, M., and Zangerl, C.: Detailed hydrogeological analysis of a deep-seated rockslide at the
968 Gepatsch reservoir (Klasgarten, Austria), Hydrogeol. J., 24, 349–371, https://doi.org/10.1007/s10040-015-1341-3, 2016.

969 Su, G. W., Geller, J. T., Pruess, K., and Hunt, J.: Overview of preferential flow in unsaturated fractures, Geophys. Monogr.
970 Ser., 122, 147–155, https://doi.org/10.1029/GM122p0147, 2000.

971 Sun, Z., Ma, R., Wang, Y., Ma, T., and Liu, Y.: Using isotopic, hydrogeochemical-tracer and temperature data to characterize
972 recharge and flow paths in a complex karst groundwater flow system in northern China, Hydrogeol. J., 24, 1393–1412,
973 https://doi.org/10.1007/s10040-016-1390-2, 2016.

974 Tallaksen, L. M.: A review of baseflow recession analysis, J. Hydrol., 165, 349–370, https://doi.org/10.1016/0022-
975 1694(94)02540-R, 1995.

976 Thompson, S. S., Kulessa, B., Essery, R. L. H., and Lüthi, M. P.: Bulk meltwater flow and liquid water content of snowpacks
977 mapped using the electrical self-potential (SP) method, The Cryosphere, 10, 433–444, https://doi.org/10.5194/tc-10-433-2016,
978 2016.

979 Tsang, C.-F., Tsang, Y. W., Birkhölzer, J., and Moreno, L.: Dynamic Channeling of Flow and Transport in Saturated and
980 Unsaturated Heterogeneous Media, in: Geophysical Monograph Series, edited by: Evans, D. D., Nicholson, T. J., and
981 Rasmussen, T. C., American Geophysical Union, Washington, D. C., 33–44, https://doi.org/10.1029/GM042p0033, 2013.

982 Vionnet, V., Brun, E., Morin, S., Boone, A., Faroux, S., Le Moigne, P., Martin, E., and Willemet, J.-M.: The detailed snowpack
983 scheme Crocus and its implementation in SURFEX v7.2, Geosci. Model Dev., 5, 773–791, https://doi.org/10.5194/gmd-5-
984 773-2012, 2012.

985 Walter, F., Amann, F., Kos, A., Kenner, R., Phillips, M., de Preux, A., Huss, M., Tognacca, C., Clinton, J., Diehl, T., and
986 Bonanomi, Y.: Direct observations of a three million cubic meter rock-slope collapse with almost immediate initiation of
987 ensuing debris flows, Geomorphology, 351, 106933–106933, https://doi.org/10.1016/j.geomorph.2019.106933, 2020.

988 Weber, S., Beutel, J., Faillettaz, J., Hasler, A., Krautblatter, M., and Vieli, A.: Quantifying irreversible movement in steep,
989 fractured bedrock permafrost on Matterhorn (CH), Cryosphere, 11, 567–583, https://doi.org/10.5194/tc-11-567-2017, 2017.

990